DOI: 10.1002/ ((please add manuscript number))

Article type: Communication

Partial-Single-Atom, Partial-Nanoparticle Composites Enhance Water Dissociation for Hydrogen Evolution

Chun Hu, Erhong Song, Maoyu Wang, Wei Chen, Fuqiang Huang, Zhenxing Feng*, Jianjun Liu*, and Jiacheng Wang*

Chun Hu, Erhong Song and Maoyu Wang contributed equally.

C. Hu, Dr. E. Song, Prof. F. Huang, Prof. J. Liu, Prof. J. Wang

State Key Laboratory of High Performance Ceramics and Superfine Microstructure

Shanghai Institute of Ceramics, Chinese Academy of Sciences

Shanghai 200050, China.

E-mail: jliu@mail.sic.ac.cn, jiacheng.wang@mail.sic.ac.cn

C. Hu, Prof. J. Liu, Prof. J. Wang

Center of Materials Science and Optoelectronics Engineering

University of Chinese Academy of Sciences

Beijing 100049, China.

M. Wang, Prof. Z. Feng

School of Chemical, Biological, and Environmental Engineering

Oregon State University

Corvallis, OR 97331, USA.

E-mail: zhenxing.feng@oregonstate.edu

C. Hu

University of the Chinese Academy of Sciences

Beijing 100049, China.

W. Chen

Department of Mechanical, Materials and Aerospace Engineering

Illinois Institute of Technology

Chicago, IL 60616, USA.

Keywords: single-atom catalyst, multiple sites, electrocatalysis, water dissociation, theoretical calculation

Abstract: The development of efficient electrocatalyst toward hydrogen evolution reaction (HER) is of significant importance in transforming renewable electricity to pure and clean hydrogen by water splitting. However, the construction of an active electrocatalyst with multiple sites that can promote the dissociation of water

molecules still remains a great challenge. Herein, we reported a partial-single-atom, partial-nanoparticle composite consisting of nanosized ruthenium (Ru) nanoparticles (NPs) and individual Ru atoms as an energy-efficient HER catalyst in alkaline medium. The formation of this unique composite mainly results from the dispersion of Ru NPs to small-size NPs and single atoms (SAs) on the Fe/N co-doped carbon (Fe-N-C) substrate due to the thermodynamic stability. The optimal catalyst exhibits an outstanding HER activity with an ultra-low overpotential (9 mV) at 10 mA cm⁻² (η₁₀), a high turnover frequency (8.9 H₂ s⁻¹ at 50 mV overpotential), and nearly 100% Faraday efficiency, outperforming the state-of-the-art commercial Pt/C and other reported HER electrocatalysts in alkaline condition. Both experimental and theoretical calculations reveal that the co-existence of Ru NPs and SAs can improve the hydride coupling and water dissociation kinetics, thus synergistically enhancing alkaline hydrogen evolution performance.

1. Introduction

Hydrogen has been regarded as an alternative to fossil fuel due to its clean and sustainable merits. Among the numerous approaches available, water electrolysis could transform the electricity from the intermittent solar and wind power to produce hydrogen. [1-3] The electrochemical hydrogen evolution reaction (HER) at the cathode is a fundamental process in water splitting. Till now, platinum (Pt) is usually recognized as the most efficient HER electrocatalyst in acid medium owing to its moderate hydrogen binding energy. [4] However, the high cost and scarcity of Pt hinder its large-scale applications. [5]

On the other hand, alkaline liquid electrolyzer technology has been commercially used because of the overall low cost of various components. Whereas, the activity of Pt in alkaline condition is about two to three orders of magnitude lower than that in acid. Previous studies have clearly expounded the significant steps in hydrogen evolution in alkaline media. The fist-step water dissociation $(H_2O + e^{-t - H^t + OH^{-tt}})$, where H^t represents adsorbed H on active site *) is followed by either Tafel step ($2H^t \rightarrow H_2$) or Heyrovsky step $(H_2O + H^t + e^{-t - H_2 + OH^{-tt}})$. [8, 9] Thus, the development of highly efficient and stable electrocatalysts that have a low water dissociation barrier as well as appropriate hydrogen adsorption/desorption strength is highly essential in

In this regard, non-Pt noble metals such as ruthenium (Ru), palladium (Pd), rhodium (Rh), have been increasingly studied due to their considerable performance for alkaline HER.^[4, 10-12] Among these metals, Ru has a comparable HER activity to Pt in alkaline medium, which has been reported in the forms of single atoms (SAs), nanoparticles (NPs), alloys, and oxides.^[4, 11, 13-16] Some researches attributed the high HER activity to Ru NPs.^[4, 17-19] For example, Baek et al. found the Ru NPs in the holes of nitrogenated carbon (Ru@C₂N) can speed the dissociation of water, which could provide more intermediate protons.^[4] Whereas, some studies indicated the remarkable performance of Ru is derived from the SAs rather than NPs.^[11, 20, 21] For instance, Chen et al. found the Ru SAs coordinated with N and C (RuC_xN_y) are more beneficial to

industrial applications.

water dissociation than Ru NPs because of the lower kinetic barrier.^[11] This inspires the idea of investigating the exact roles of Ru NPs and SAs in alkaline HER.

Herein, we designed a partial-single-atom, partial-nanoparticle nanocomposite *via* the coupling of Ru SAs and Ru NPs on the Fe/N co-doped carbon (Fe-N-C) substrate, and further evaluated the influence of both SAs and NPs on the HER performance. The existence of Fe SAs coordinated with N groups (Fe-N) in the carbon matrix could disperse the large-sized Ru NPs into Ru SAs stabilized by N groups (Ru-N₄) and smaller Ru NPs. Moreover, the Fe-N groups could effectively adjust the electronic distribution of these Ru NPs, thus achieving the optimal ΔG_{H^*} . Density functional theory (DFT) simulation reveals that, the Ru-N₄ SA moieties facilitate the splitting of water molecules and the generation of hydrogen adsorbates that then recombine into hydrogen molecules on the nearby smaller Ru NPs. Both of the Ru SAs with a low water dissociation barrier and Ru NPs with a proper hydrogen adsorption/desorption strength synergistically enhance hydrogen evolution performance in alkaline condition.

2. Results and discussion

2.1. Synthesis and structural identification

Generally, the size and placement of metal NPs can generate distinct catalytic activity.
[11, 20, 22] In this work, we prepared the Ru/C, Ru/N-C and Ru/Fe-N-C nanocomposites
via a two-step process (see details in Experimental), as shown in **Figure 1**a. Abundant
voids originating from the removal of colloidal silica were observed in Ru/Fe-N-C
(Figure S2). The resulting Ru/Fe-N-C consists of C, N, Fe, and Ru elements, as well

as a small amount of O element derived from trapped moisture and/or edged oxygencontaining groups (Figure S3 and Table S1). Ultrafine Ru NPs are dispersed within porous Fe-N-C matrix (Figure S4). The lattice spacing of Ru NPs is 0.232 and 0.212 nm, which is attributed to the (100) and (002) planes of Ru, respectively (Figure 1b). There are many Ru SAs around Ru NPs (Figure 1c and Figure S5), and this has also been observed in the previous research. [11, 20] The Ru content of Ru/Fe-N-C is 4.92 wt. %, determined by the inductively coupled plasma (ICP) analysis. The N₂ adsorption/desorption measurements confirm a narrow mesopore size distribution, a large surface area of 810 m²/g and pore volume of 1.8 cm³/g for Ru/Fe-N-C (Figure S6 and Table S2). With the increasing of Ru content, the particle size of Ru becomes larger (Figure S7). The high-angle annular dark-field scanning transmission electron microscopy (HAADF-STEM) image and the corresponding energy dispersive X-ray (EDX) mapping were employed to analyze the distribution of Ru, Fe, N, and C elements. The Fe component is either abundant (zone I) or deficient (zone II) around Ru NPs (Figure 1d), and N moiety is homogeneously distributed within the carbon matrix. Furthermore, no aggregated Fe particles are observed (Figure 1d), so as to Rufree Fe-N-C sample (Figure S8-10).

To further understanding of the Ru structure, Ru K-edge X-ray absorption spectroscopy (XAS) was performed (Figure S12).^[23, 24] As shown in Figure 1e, the Fourier-transform Ru K-edge extended X-ray absorption fine structure (EXAFS) of Ru/Fe-N-C exhibits two main peaks. The peak of ~1.5 Å is Ru-N/C scattering due to the existing of Ru SAs,^[16] and the other at ~2.4 Å is associated with Ru-Ru scattering

caused by the formation of Ru NPs. Meanwhile, Ru/Fe-N-C has a smaller size of Ru NPs than Ru/N-C, as reflected by the lower Ru-Ru scattering intensity. ^[25, 26] Specifically, model-based EXAFS fitting further reveals that the ratio of Ru-Ru between Ru/N-C and Ru/Fe-N-C is ~2.17 (Figure S13-14 and Table S3), which confirms the larger cluster size in Ru/N-C. From the EXAFS fitting result for Ru/Fe-N-C, we notice that the Ru-N coordination is over-saturated (higher than 4 in coordination number) even considering the EXAFS fitting error if we don't include any Ru-Fe bond (Ru-Fe interaction), as shown in Figure S13 and Table S3. We believe that the Ru NPs could be not simply dispersed on the Fe-N-C surface, and it should interact with Fe-N species. The wavelet transfer of Ru K-edge EXAFS confirms that there is some other Ru-scattering around 2.4 Å instead of only Ru-Ru scattering which could be Ru-Fe (Figure 1f). When including the Ru-Fe bonds in our model, the fitting quality for Ru/Fe-N-C EXAFS is much improved (Figure S13 and Table S3).

To identify the most possible atom-dispersion structure, a series of RuN_xC_y configurations (x+y≤4) including 2, 3, or 4 coordinates were calculated by using DFT method. Their structural stability is determined by comparing their formation energies of single Ru insertion into different defected configurations (Figure 1g, Figure S19 and Table S4). The formation energies of RuN_xC_y (x+y≤4) are in agreement with the previously reported results. [11, 21, 27, 28] The calculation results also explain the experimental observation of Ru-N and Ru-C bonding.

On the other hand, to eliminate the influence of Ru element, HAADF-STEM and electron energy loss spectroscopic (EELS) measurements were conducted in pure Fe-N-C samples. As shown in Figure 1h, Fe exists in the formation of single atomic configurations. Quantitative analysis of Fourier transformed Fe K-edge EXAFS further reveals the presence of Fe SA sites in Fe-N-C. Since it is hard for EXAFS to distinguish the elements that are close in atomic number, we start with DFT-suggested best models to refine the EXAFS results, and in turn these fitted parameters will feed back to DFT to further confirm the local configurations. In addition, the previous literatures^[29-32] suggest that Fe prefers to form SA sites anchored on N for high activity. Finally, the model-based fitting of Fe with standard FeN₄ structure reproduce our EXAFS spectrum perfectly, which gives a mean bond length of 2.03 ± 0.02 Å for Fe-N. The Fe-N bond length in Ru/Fe-N-C is evidently longer than that in Fe-N-C, which may originate from strong interaction of Ru NPs and Fe-N group (Figure 1i). Based on the interaction of Ru NPs and Fe-N from our above discussions, the second scattering peak in wavelet transfer Ru EXAFS is assigned to Ru-Fe scattering. To elucidate interaction mechanism of Ru NPs with different moieties in carbon substrate, we calculated the average formation energies of three simulated structures (i.e. Ru/C, Ru/N-C and Ru/Fe-N-C). HAADF-STEM image of Ru/Fe-N-C estimates the average size of Ru NPs is around 1.8 nm, and the average Ru-Ru coordinate is around 4. Combining with the Ru NPs information from the previous studies, [33] we built a Ru₆ NP in octahedron configuration with adjacent Fe atoms (Figure 1j). The theoretical model was used to fit Ru/Fe-N-C EXAFS again (Figure S13), which

shows more reasonable fitting results with four-coordinated Ru-N (Table S3). The new fitting results imply that the Ru-Ru coordination ratio between Ru/N-C and Ru/Fe-N-C is still 2.17. Applying the same strategy in our previous study, [26] we use this ratio to scale up the size of NPs in Ru/N-C, and the result matches well with the size of Ru₁₃ with dodecahedron structure reported before. [33] Based on the formula of $\Delta E^{atom} = (E^{atom-NCS} - N^{atom}E^{atom})/N^{atom}$, as shown in Figure 1j and Table S5, the Ru₆ octahedron configuration on Fe-N₄ carbon substrate is preferentially formed with the lowest value for average formation energy. Both the experimental and theoretical results show that the smaller metal NPs thermodynamically prefer to form on the Fe-N₄ substrate.

2.2. Electrochemical HER performance

To investigate the effect of the Ru SAs and Ru NPs on the HER activity, the performance of Ru/Fe-N-C and the control samples was firstly evaluated in 1 M KOH electrolyte by a three-electrode electrochemical cell. The HER activity was normally evaluated by the overpotential (η_{10}) versus reversible hydrogen electrode (RHE) at a current density of 10 mA cm⁻², and it is the current density for an expected 12.3% solar water-splitting conversion efficiency.^[34] As shown in **Figure 2**a, no evident cathodic current is observed for pure Fe-N-C. However, the synergy of Ru with the Fe-N-C matrix shows an outstanding HER activity with a very small onset potential at the thermodynamic potential (i.e. 0 V), demonstrating that Ru is indispensable in boosting the HER activity. It exhibits a very low η_{10} value of \sim 9 mV, even 25 mV

smaller than commercial Pt/C (~34 mV). Normalized to respective loading, Ru/Fe-N-

C shows a large mass activity (-2.56 A mg_{Ru}^{-1}), which is 3.3 times higher than

commercial Pt/C (-0.78 A mg_{Pt}^{-1}) at 50 mV (Figure S20). To highlight the key role of Fe and N in HER, N-Fe-free Ru/C and Fe-free Ru/N-C were also prepared (see Supporting Information), both of which possess similar pore textures as Ru/Fe-N-C (Figure S2). Although N-doping leads to a smaller η_{10} value (64 mV) for Ru/N-C than 85 mV for Ru/C, both of them are far larger than 9 mV for Ru/Fe-N-C, as shown in the obvious negative shift of the polarization curves (Figure 2a). These results reveal the significant roles of both Ru SAs and Ru NPs in improving the HER activity of Ru/Fe-N-C. Notably, the HER activity of present Pt/C is among the best in the previous reports, [14, 17, 19] which indicates the excellent intrinsic activity for Ru/Fe-N-C, not resulting from the use of a poor Pt/C reference.

Tafel slope reflects the interfacial kinetics, and HER involves either the Volmer-Heyrovsky or the Volmer-Tafel mechanism. [18, 35-37] The doping of active Fe-N sites into substrate results in a significant decrease of Tafel slope from 62 and 68 mV dec⁻¹ for Ru/N-C and Ru/C to 28 mV dec⁻¹ for Ru/Fe-N-C, respectively. The value is even 5 mV dec⁻¹ smaller than that of Pt/C (Figure 2b), suggesting a Volmer-Tafel mechanism for Ru/Fe-N-C. The exchange current density (J₀) was obtained by extrapolating the Tafel plots. As shown in Figure S21, Ru/Fe-N-C possesses a J₀ of 1.94 mA cm⁻², which is much higher than other contrast catalysts, and even surpasses Pt/C.

Moreover, Ru/Fe-N-C gives the highest specific current density of 0.0156 mA cm⁻² (-0.05 V vs. RHE), which is 4, 10.4, 18.1, 312 times higher than Pt/C (0.0039 mA cm⁻²), Ru/N-C (0.0015 mA cm⁻²), Ru/C (0.0086 mA cm⁻²), Fe-N-C (0.00005 mA cm⁻²), respectively (Figure 2c). Electrochemical impedance spectroscopy (EIS, -0.1 V vs. RHE) of Ru/Fe-N-C exhibits the smallest semicircle, which indicates the intrinsic fast charge transfer at the interface of electrocatalyst and electrolyte (Figure 2d). These results demonstrate that the HER kinetics are sharply enhanced by anchoring both Ru SAs and NPs on Fe-N-C substrate.

The electrochemical double-layer capacitance (C_{dl}) is another effective technique to estimate the electrochemically active surface area (ECSA) of samples with similar structures and compositions. ^[38, 39] The C_{dl} values were obtained by use of cyclic voltammetry versus scan rates (Figure S22). As depicted in Figure 2e, the C_{dl} value follows the order as Fe-N-C (8.87 mF cm⁻²) < Ru/C (9.27 mF cm⁻²) < Ru/N-C (38.11 mF cm⁻²) < Ru/Fe-N-C (53.06 mF cm⁻²). The larger C_{dl} , the better proton exchangeability between active sites and electrolyte. Thus, the above results show the optimized chemical composition of Ru/Fe-N-C for HER with enhanced activity when compared to Ru/C and Ru/N-C. The Ru/Fe-N-C exhibits a neglectable increase of η_{10} after 5000 CV tests, while commercial Pt/C shows a larger degradation of ~15 mV under the similar condition (Figure 2f). And the HRTEM characterizations confirm that the morphology has no evident change after long-term operation (Figure S23), revealing the remarkable stability of Ru/Fe-N-C. This is possibly attributed to strong coupling of Ru and Fe-N-C matrix, that keeping it from reconstruction. The Ru/Fe-N-C matrix, that keeping it from reconstruction.

C also exhibits high durability of oxidation-resistance, and the valence state of Ru remains unchanged after long-term exposure to air (Figure S24). Subsequently, gas chromatography was employed to detect the H₂ production, which shows that the Faradaic efficiency of Ru/Fe-N-C is nearly 100% under a wide range of potentials (Figure 2g and Figure S25). In terms of η_{10} (9 mV) and Tafel slope (28 mV dec⁻¹), Ru/Fe-N-C outperforms or is comparable to the state-of-the-art metal-based HER electrocatalysts including NiFeRu-LDH (29 mV, 31 mV dec⁻¹), [40] A-CoPt-NC (50 mV, 48 mV dec⁻¹), [41] Ru@C₂N (17 mV, 38 mV dec⁻¹), [4] Ru₂P/NPC (52 mV, 69 mV dec⁻¹), [42] Ru@CQDs (10 mV, 47 mV dec⁻¹), [19] RuCo@NC (28 mV, 31 mV dec⁻¹)[14], Ru@CN (32 mV, 53 mV dec⁻¹)^[17], RuSAs + RuNPs@MHC (7 mV, 29 mV dec⁻¹)^[43], and Cu/Ru@G_N (8 mV, 29 mV dec⁻¹)[44] (Figure 2h and Table S6). Turnover frequency (TOF) is the most effective figure of merit to characterize intrinsic electrocatalytic activity of catalysts. The number of active sites for Ru/Fe-N-C and Pt/C were estimated by means of Cu underpotential deposition (UPD) (Figure S26). As illustrated in Figure 2i and Table S7, Ru/Fe-N-C gives a TOF value of 3.6 H₂ s⁻¹ and 8.9 H₂ s⁻¹ at an overpotential of 25 mV and 50 mV, respectively, which is 7.6 and 6.1 times larger than that of Pt/C (0.47 H₂ s⁻¹ at 25 mV overpotential and 1.46 H₂ s⁻¹ at 50 mV overpotential). In addition, the TOF value of Ru/Fe-N-C significantly exceeds those of Ru-based catalysts, such as Ru@C₂N (0.76 H₂ s⁻¹ at 25 mV overpotential; $1.66 \text{ H}_2 \text{ s}^{-1}$ at 50 mV overpotential), [4] Ru/NC (4.55 H₂ s⁻¹ at 100 mV overpotential), [21] and is also superior than those of α -Mo₂C (0.9 H₂ s⁻¹ at 200 mV overpotential), [45] γ -

 Mo_2N (0.07 H_2 s⁻¹ at 250 mV overpotential), $^{[45]}$ Ni_5P_4 (2.9 H_2 s⁻¹ at 200 mV overpotential), $^{[46]}$ Ni-Mo (0.05 H_2 s⁻¹ at 100 mV overpotential). $^{[47]}$

2.3. Effect of substrates

In order to further understand the origin of high HER activity of Ru/Fe-N-C with both Ru SAs and Ru NPs, the influence of various substrates on Ru moieties was investigated in detail by X-ray photoelectron spectroscopy (XPS), X-ray absorption spectroscopy (XAS) and DFT calculations. Ru 3p XPS core-level spectra show that the peaks at ~462.2 and ~484.4 eV are allocated to the Ru⁰ moiety and the other peaks are Ruⁿ⁺ in three samples (Figure 3a). Ru/Fe-N-C has the highest content of Ruⁿ⁺ (~32%), which can be attributed to the strong interaction between Ru NPs and Fe-N-C substrate, as well as the high density of Ru SAs coordinated with C/N groups (Figure 3b and 1e). The Fe2p exhibits a negative shift by ~0.6 eV after Ru loading (Figure S29), implying the increased electron transfer of Ru NPs to the Fe-N-C substrate. The identical result is attained in the XAS measurement as well. The negative shift to lower energy region is shown in the Fe K-edge XANES spectra when Ru species were incorporated, suggesting a more reduced valence state of Fe in Ru/Fe-N-C than that in pure Fe-N-C (Figure 3c). The Ru K-edge XANES curves reveal the absorption edge of Ru/Fe-N-C is higher than Ru/N-C, and a special valence state of +2.4 is obtained for Ru in Ru/Fe-N-C sample (Figure 3d-e). Associated with the Ru EXAFS results (Figure 1e), such a high valence state of Ru in Ru/Fe-N-C may derive from the synergetic effect of Ru SAs and small-sized Ru NPs. The well consistence of XPS

and XANES effectively confirms the strong electronic interaction between Ru and Fe-N-C support, and it may account for the fact of ultrahigh HER activity. To further identify the charge transfer between Ru NPs and various carbon substrates, we also calculated the Bader charge of Ru/C, Ru/N-C and Ru/Fe-N-C system. From the quantitative (Figure 3f and Table S5) and qualitative analysis (Figure 3g-i) of charge transfer based on DFT calculation, it is found that Fe-N-C substrate prefers to regulating the electron structure of Ru NPs with the largest amount of charge transfer when comparing with other substrates.

2.4. Understanding the origin of high activity by DFT calculation

To understand catalytic role of multiple active sites and construct a unified picture, density functional theory (DFT) calculations were performed to investigate catalytic sites and corresponding energetics of Ru/C, Ru/N-C, and Ru/Fe-N-C. The hydrogen adsorption free energy ΔG_{H^*} is an effective descriptor to determine the HER activity, while water dissociation barrier of catalysts is considered as an important parameter to estimate the catalytic activity. Since Ru/Fe-N-C exhibits highly active catalysis by experiment, different atomic sites of Ru cluster in Ru/Fe-N-C were used to calculate ΔG_{H^*} (**Figure 4**a). The Ru atoms located from faraway to connecting with Fe-N-C exhibit an increasing hydrogen adsorption energy, ΔG_{H^*} (Ru1) =0.025 eV and ΔG_{H^*} (Ru3) =-0.403 eV. The optimal HER active site is considered as Ru1 (Figure 4b). For comparison, we also calculated ΔG_{H^*} of Ru₆ nanoparticle without substrate with the strong hydrogen binding energy (-0.37 eV), which is unfavorable for

hydrogen desorption. In general, the different catalytic activity is attributed to oxidization degree of different atoms of Ru NP on substrate. The Bader charge calculations show about 0.989 e⁻ charge transfer from Ru NPs to Fe-N₄ entity. In comparison, the atoms connected with Fe-N-C substrate have stronger charge transfer than those faraway Ru atoms. The structure-property relationship is also exhibited in the various atoms of Ru/N-C and Ru/C system (Figure S30).

It is widely accepted that hydrogen evolution in alkaline contains two continuous steps of water dissociation and hydrogen desorption. Besides hydrogen desorption, the barrier height (ΔG_B) of water dissociation also plays an important role in determining overall alkaline HER reaction kinetic rate. Based on our DFT calculations, it is found that two active sites of Ru-N₄ and Ru3 of Ru cluster in Ru/Fe-N-C system exhibit much lower activation barriers (0.550 eV and 0.774 eV) for water dissociation, respectively, than Pt catalysis (0.94 eV).^[18] From the kinetic viewpoints, atom-dispersed Ru-N₄ could accelerate water dissociation to provide neutral hydrogen source. Furthermore, the atom-dispersed Ru also has appropriate hydrogen binding energy. Thus, the atom-dispersed Ru is of much importance to high-efficiency HER in alkaline media (Figure 4c and Figure S31-32).

Higher hydrogen binding energy corresponds to higher activity of water dissociation, but lower hydrogen desorption capacity. As shown in Figure 4d, there is a linear correlation between and among ΔG_{H^*} , Ru-H bond length and the amount of charge transfer Δe^- , indicating the more active electron transfer and the stronger hydrogen binding energy. The similar correlation is further verified by the

relationship between the Ru-H bond length and charge transfer Δe^{-} . Furthermore, we also studied the projected density of state (pDOS) of various Ru sites in Ru/Fe-N-C system to understand the origin of high activity (Figure 4e). Through comparing Ru1-4d, Ru2-4d and Ru3-4d active electron density near Fermi (highlighted by yellow rectangular areas), it is observed that the amounts of electron states 4d orbitals of Ru1-3 atom between -1 and 0 eV gradually increase corresponding to the intensity of hydrogen binding from weak to strong. The pDOS before and after H absorbed of Ru/C and Ru/N-C system are illustrated in Figure S33. Moreover, compared to ΔG_{H^+} of Ru/C and Ru/N-C system (Figure 4f), the Fe-N-C substrate prefers to regulate the intrinsic charge distribution of Ru NPs, further optimizing the HER performance.

3. Conclusion

In summary, we prepared an efficient hydrogen evolution catalyst by combining Ru SAs with Ru NPs on the Fe/N co-doped carbon substrate (Fe-N-C). The resulting Ru/Fe-N-C catalyst exhibits markedly enhanced reaction kinetics, large mass and BET surface area activity, as well as high intrinsic activity (TOF) for HER. Theoretical calculations suggest that the single atom Ru-N₄ moieties could significantly improve the water dissociation kinetics, while the Ru NPs are beneficial to hydrogen evolution. We found that the incorporation of Fe species could promote Ru NPs into isolated Ru atoms and small-sized Ru NPs. Moreover, the Fe-N-C substrate could further adjust the charge distribution of Ru NPs, thus optimizing the hydrogen adsorption energy. This study demonstrates the potential of special substrate

in modifying particle size and electronic structure of metal NPs, paving a new avenue for designing efficient electrocatalysts in erergy conversion and storage.

4. Experimental Section

Chemical reagents: All chemicals, including ruthenium chloride hydrate (Aladdin, 35.0-42.0 wt.% Ru basis), D (+)-glucose monohydrate (Sinopharm Chemical Reagent Co., Ltd.), dicyandiamide (Aladdin, 99%), Ludox HS40 colloidal silica (Aldrich, 40 wt.%), iron chloride anhydrous (Sinopharm Chemical Reagent Co., Ltd.), potassium hydroxide (Sinopharm Chemical Reagent Co., Ltd., ≥85%), sodium hydroxide (Sinopharm Chemical Reagent Co., Ltd.), potassium phosphate monobasic (Aladdin, ≥99%), Nafion solution (Sigma-Aldrich, 5 wt.%), Pt/C catalyst (Johnson Matthey, 40 wt.%) and concentrated sulfuric acid (Sinopharm Chemical Reagent Co., Ltd., 95~98%), were used as received without further purification.

Materials synthesis: The Ru nanoparticles anchored onto a Fe-N-C support (Ru/Fe-N-C) with uniform mesopores were prepared *via* a pyrolysis and subsequent etching strategy. Typically, a certain amount of glucose (2 g), dicyandiamide (2 g), iron chloride anhydrous (0.3 g) and 8 g colloid silica solution were mixed with 50 mL deionized water under vigorously stirring to get a homogeneous mixed solution, followed by the addition of 20 mL ruthenium chloride aqueous solution (0.048 mM). After stirring for ~30 min, the mixture was evaporated by heating up to 110 °C and maintained at this temperature under continuously stirring. The dried brown product was pyrolyzed at 800 °C for 2 h in quartz tube furnace under Ar atmosphere with a heating rate of 5 °C min⁻¹. After cooling, the silica template was etched off with 2 M

NaOH solution. After being rinsed several times with deionized water and ethanol, the black solid was further leached in 0.5 M H₂SO₄ at 60 °C for 2 h to remove the unstable iron-containing species. Finally, the catalyst was collected by centrifugation and purified by deionized water and ethanol for several times, and then dried under oven at 90 °C. The resultant dark solid, named as Ru/Fe-N-C, was ground into a fine powder for further analyses. The control samples of Fe single atom coordinated with pyridinic-N-doped carbon framework (Fe-N-C), Ru nanoparticles supported on carbon (Ru/C), and Ru nanoparticles dispersed within N-doped carbon matrix (Ru/N-C) were prepared using the same process. Specifically, Fe-N-C was prepared without the addition of Ru source, Ru/C was prepared in the absence of Ru, Fe, and N sources, and Ru/N-C was synthesized without adding Fe source. Other samples possess diverse ruthenium content were labeled as Rux/Fe-N-C (x=0.05, 0.1, 0.3).

Structural characterization: A JEOL S-4800 SEM was used to characterize the sample morphology. Samples for analysis were mounted onto a conductive carbon double-sided sticky tape. TEM measurement was performed employing a JEOL JEM-2100F microscope operating at an accelerating voltage of 200 kV. Samples were deposited on a thin amorphous porous carbon film supported by copper grid derived from ultrasonic ethanol solutions. High-resolution TEM (HRTEM) was performed on JEM-ARM300F at an acceleration voltage of 300 kV with an EDS attachment. The XRD patterns were collected on a Bruker D8 ADVANCE diffraction workstation with Cu Kα radiation. Raman spectroscopy were performed using a DXR Raman Microscope (Thermal Scientific Co., USA) with 532 nm excitation wavelength.

Nitrogen adsorption-desorption measurements were conducted at -196 °C on a Quadrasorb SI surface area and pore sizes analyzer (Quantachrome Ins). The specific surface area and pore sizes were calculated based on the Brunauer-Emmett-Teller (BET) and Barrett-Joyner-Halenda (BJH) methods, respectively. All samples were dehydrated under vacuum at 200 °C overnight before each measurement. XPS characterizations were carried out on an ESCALAB 250Xi X-ray photoelectron spectrometer (Thermal Scientific Co., USA) with Al Kα radiation. The elemental spectra were all calibrated with respect to C1s peaks at 284.8 eV. The Ru metal content of the catalysts was measured by inductively coupled plasma atomic emission spectroscopy (ICP-AES). A certain amount of sample was mixed with 5 ml nitric acid, which was transferred to high pressure digestion tank, sealed and remained at 235 °C for 10 h. Subsequently, 5 ml hydrochloric acid was added in above mixture, heating until the sample is completely dissolved. And the resulting solution was examined by using iCAP 6300 spectrometer. X-ray absorption fine-structure spectroscopy (XAFS) was performed the Advanced Photo Source at Argonne National Laboratory at the 5-BM beamline. The nanoparticle samples were drop cast onto Kapton tape and measured from 150 eV below the K-edge absorption of Fe (7.11 keV) or Ru (22.10 keV) to 800 eV above the respective absorption edges. Metal foils of either Fe or Ru were used to calibrate E₀ and served as reference material for subsequent linear combination fitting of the X-ray absorption near-edge structure (XANES). All data processing and linear combination fitting were performed using the software program Athena.

Electrochemical measurements: The electrochemical measurements were carried out in a three-electrode setup using a CHI 760C workstation at room temperature. To prepare the working electrode, 5 mg electrocatalyst and 25 μL Nafion solution were dispersed in 500 μL of 1:1 (v:v) water/ethanol by sonication to form a homogeneous ink. Then, 10 μL suspension was loaded onto a 5 mm diameter polished glassy carbon electrode (catalyst loading amount ~0.485 mg cm²). A graphite rod and saturated calomel electrode (SCE) were used as the counter electrode and reference electrode, respectively. The reference electrode was experimentally calibrated against RHE. Linear sweep voltammetry (LSV) was conducted in 1.0 M aqueous KOH with a scan rate of 2 mV s⁻¹ and a rotation speed of 1600 rpm. Commercial 20 wt% Pt/C was used as a reference to evaluate the electrocatalytic performance of as-prepared catalysts. The cyclic voltammetry (CV) measurements were conducted at 1600 rpm with a sweep rate of 100 mV s⁻¹ for 5000 times to investigate the cycling stability.

Calculation of the turnover frequency (TOF): The number of active sites (n) was qualified by using the copper underpotential deposition (Cu UPD) with the following equation:^[4]

$$n = \frac{Q_{Cu}}{2F} \tag{1}$$

where Q_{Cu} is the copper stripping charge, and F is the faraday constant (96485 C mol⁻¹).

The TOF was calculated with the following equation:

$$TOF = \frac{I}{2Fn} \tag{2}$$

The factor 1/2 is based on the consideration that two electrons are required to form one hydrogen molecule.

Faradaic efficiency measurements: Faradaic efficiency (FE) of Ru/Fe-N-C was measured at different potentials (-0.05, -0.10, -0.15, -0.20 V vs. RHE) by gas chromatography (7820A, Agilent), and a thermal conductivity detector (TCD) was used for H₂ quantification. In a custom-made two compartment cell (single cell: 50 mL) separated by a Nafion 117 membrane, each compartment of the cell was filled with 35 mL 1.0 M KOH. 20 μL suspension was droped onto a 1×1 cm² diameter carbon cloth electrode (catalyst loading amount ~0.97 mg cm²). The H₂ gas was purged out from the cell by using 1 mL syringe and injected into GC. FE was calculated according to following relationship:^[49]

$$FE = \frac{2F \cdot n_{H_2}}{Q} \tag{3}$$

where is n_{H_2} is the amount of hydrogen (mol), and Q is the total amount of charge passed through the cell (C).

Theoretical calculations: Spin-polarized density functional theory (DFT) calculations were performed using the Vienna Ab initio Simulation Package (VASP) plane-wave DFT code, with the generalized gradient approximation of Perdew-Burke-Ernzerhof to describe electron exchange and correlation. The plane-wave basis is cut off by 500 eV. The projector-augmented plane wave (PAW) was used to describe the electron-ion interactions. A set of (3×3×1) k-points were carried out for geometric optimization, and the convergence threshold was set as 10⁻⁴ eV in energy and 0.05 eV/Å in force, respectively. The Hubbard-type U correction for the strong-correlation d-electrons of transition metals are taken into account. To calculate transition

barriers, it is performed climbing image nudge elastic band calculations^[54] on each of these combinations of the final H+OH configuration with the most stable initial H₂O configuration and selected the combination with the least energy barrier for each surface.

For the systems, the free energy of the adsorbed state is calculated as:

$$\Box \triangle G_{H^*} = \triangle E_{H^*} + \triangle E_{ZPE} - T \triangle S \tag{4}$$

where $\triangle E_{H^*}$ is the hydrogen chemisorption energy, and $\triangle E_{ZPE}$ is the difference corresponding to the zero point energy between the adsorbed state and the gas phase. As the vibration entropy of H* in the adsorbed state is small, the entropy of

adsorption of 1/2 H₂ is $\triangle S_H \approx -1/2 S_{H_2}^0$, where $S_{H_2}^0$ is the entropy of H₂ in the gas phase at the standard conditions.

Supporting Information

Supporting Information is available from the Wiley Online Library or from the author.

Acknowledgements

The authors are grateful to the financial support from Science and Technology Commission of Shanghai Municipality (19ZR1465100, 19ZR1479500), Equipment Research Program (6140721050215), National Natural Science Foundation of China (No. 21973107, and 51702345), and the Science & Technology Innovation Major Program of Ningbo (Ningbo 2025 Program, 2018B10056). J.W. thanks the Program of Shanghai Academic Research Leader (20XD1424300) for financial support. W.C. acknowledges the support from U.S. National Science Foundation (NSF) under the CAREER award DMR-1945380. Z.F. thanks the startup financial support from Oregon State University. XAS measurements were done at 5-BM-D of DND-CAT, which is supported through E. I. duPont de Nemours & Co., Northwestern University, and The Dow Chemical Company. The use of APS of ANL is supported by DOE under Contract No. DE-AC02–06CH11357.

Received: ((will be filled in by the editorial staff))

Revised: ((will be filled in by the editorial staff))

Published online: ((will be filled in by the editorial staff))

References

- [1] Z. W. Seh, J. Kibsgaard, C. F. Dickens, I. Chorkendorff, J. K. Norskov, T. F. Jaramillo, *Science* **2017**, *355*, eaad4998.
- [2] I. Roger, M. A. Shipman, M. D. Symes, Nat. Rev. Chem. 2017, 1, UNSP 0003.
- [3] S. Chu, A. Majumdar, *Nature* **2012**, *488*, 294.
- [4] J. Mahmood, F. Li, S. M. Jung, M. S. Okyay, I. Ahmad, S. J. Kim, N. Park, H. Y. Jeong, J. B. Baek, *Nat. Nanotechnol.* **2017**, *12*, 441.
- [5] J. N. Tiwari, S. Sultan, C. W. Myung, T. Yoon, N. Li, M. Ha, A. M. Harzandi, H. J. Park, D. Y. Kim, S. S. Chandrasekaran, W. G. Lee, V. Vij, H. Kang, T. J. Shin, H. S. Shin, G. Lee, Z. Lee, K. S. Kim, *Nat. Energy* **2018**, 3, 773.
- [6] K. Zeng, D. Zhang, *Prog. Energy Combust. Sci.* **2010**, *36*, 307.
- [7] P. J. Rheinl ander, J. Herranz, J. Durst, H. A. Gasteiger, *J. Electrochem. Soc.* **2014**, *161*, F1448.
- [8] R. Subbaraman, D. Tripkovic, K. C. Chang, D. Strmcnik, A. P. Paulikas, P. Hirunsit, M. Chan, J. Greeley, V. Stamenkovic, N. M. Markovic, *Nat. Mater.* **2012**, *11*, 550.
- [9] D. Strmcnik, P. P. Lopes, B. Genorio, V. R. Stamenkovic, N. M. Markovic, *Nano Energy* **2016**, *29*, 29.
- [10] T. Bhowmik, M. K. Kundu, S. Barman, ACS Catal. 2016, 6, 1929.
- [11] B. Lu, L. Guo, F. Wu, Y. Peng, J. E. Lu, T. J. Smart, N. Wang, Y. Z. Finfrock, D. Morris, P. Zhang, N. Li, P. Gao, Y. Ping, S. Chen, *Nat. Commun.* **2019**, *10*, 631.
- [12] L. Zhu, H. Lin, Y. Li, F. Liao, Y. Lifshitz, M. Sheng, S. T. Lee, M. Shao, *Nat. Commun.* **2016**, *7*, 12272.
- [13] T. Bhowmik, M. K. Kundu, S. Barman, ACS Appl. Mater. Inter. 2016, 8, 28678.
- [14] J. Su, Y. Yang, G. Xia, J. Chen, P. Jiang, Q. Chen, Nat. Commun. 2017, 8, 14969.
- [15] J. Ding, Q. Shao, Y. Feng, X. Huang, *Nano Energy* **2018**, *47*, 1.
- [16] P. Li, M. Wang, X. Duan, L. Zheng, X. Cheng, Y. Zhang, Y. Kuang, Y. Li, Q. Ma, Z. Feng, W. Liu, X. Sun, *Nat. Commun.* **2019**, *10*, 1711.
- [17] J. Wang, Z. Wei, S. Mao, H. Li, Y. Wang, Energ. Environ. Sci. 2018, 11, 800.
- [18] Y. Zheng, Y. Jiao, Y. Zhu, L. H. Li, Y. Han, Y. Chen, M. Jaroniec, S. Z. Qiao, *J. Am. Chem. Soc.* **2016**, *138*, 16174.
- [19] W. Li, Y. Liu, M. Wu, X. Feng, S. A. T. Redfern, Y. Shang, X. Yong, T. Feng, K. Wu, Z. Liu, B. Li, Z. Chen, J. S. Tse, S. Lu, B. Yang, *Adv. Mater.* **2018**, *30*, e1800676.
- [20] J. N. Tiwari, A. M. Harzandi, M. Ha, S. Sultan, C. W. Myung, H. J. Park, D. Y. Kim, P. Thangavel, A. N. Singh, P. Sharma, S. S. Chandrasekaran, F. Salehnia, J. W. Jang, H. S. Shin, Z. Lee, K. S. Kim, *Adv. Energy Mater.* **2019**, *9*, 1900931.

- [21] J. Zhang, P. Liu, G. Wang, P. P. Zhang, X. D. Zhuang, M. W. Chen, I. M. Weidinger, X. L. Feng, *J. Mater. Chem. A* **2017**, *5*, 25314.
- [22] J. Yu, Y. Guo, S. She, S. Miao, M. Ni, W. Zhou, M. Liu, Z. Shao, *Adv. Mater.* **2018**, *30*, e1800047.
- [23] Z. Feng, Q. Ma, J. Lu, H. Feng, J. W. Elam, P. C. Stair, M. J. Bedzyk, *RSC Advances* **2015**, *5*, 103834.
- [24] M. Wang, L. Árnadóttir, Z. J. Xu, Z. Feng, *Nano-Micro Lett.* **2019**, *11*, 47.
- [25] A. I. Frenkel, A. Yevick, C. Cooper, R. Vasic, Annu. Rev. Anal. Chem. 2011, 4, 23.
- [26] Z. Weng, Y. Wu, M. Wang, J. Jiang, K. Yang, S. Huo, X. F. Wang, Q. Ma, G. W. Brudvig, V. S. Batista, Y. Liang, Z. Feng, H. Wang, *Nat. Commun.* **2018**, *9*, 415.
- [27] X. Wang, W. Chen, L. Zhang, T. Yao, W. Liu, Y. Lin, H. Ju, J. Dong, L. Zheng, W. Yan, X. Zheng, Z. Li, X. Wang, J. Yang, D. He, Y. Wang, Z. Deng, Y. Wu, Y. Li, *J. Am. Chem. Soc.* **2017**, *139*, 9419.
- [28] C. Zhang, J. Sha, H. Fei, M. Liu, S. Yazdi, J. Zhang, Q. Zhong, X. Zou, N. Zhao, H. Yu, Z. Jiang, E. Ringe, B. I. Yakobson, J. Dong, D. Chen, J. M. Tour, *ACS Nano* **2017**, *11*, 6930.
- [29] X. Wan, X. Liu, Y. Li, R. Yu, L. Zheng, W. Yan, H. Wang, M. Xu, J. Shui, *Nat. Catal.* **2019**, *2*, 259.
- [30] K. Yuan, S. Sfaelou, M. Qiu, D. Lützenkirchen-Hecht, X. Zhuang, Y. Chen, C. Yuan, X. Feng, U. Scherf, *ACS Energy Lett.* **2017**, *3*, 252.
- [31] Q.-L. Zhu, W. Xia, L.-R. Zheng, R. Zou, Z. Liu, Q. Xu, ACS Energy Lett. 2017, 2, 504.
- [32] A. Zitolo, V. Goellner, V. Armel, M. T. Sougrati, T. Mineva, L. Stievano, E. Fonda, F. Jaouen, *Nat. Mater.* **2015**, *14*, 937.
- [33] G. Zhang, H. Zhao, L. Wang, J. Phys. Chem. B 2004, 108, 2140.
- [34] C. Wei, Z. J. Xu, Small Methods 2018, 2, 1800168.
- [35] S. A. Vilekar, I. Fishtik, R. Dattaz, J. Electrochem. Soc. 2010, 157, B1040.
- [36] T. Ling, D. Y. Yan, H. Wang, Y. Jiao, Z. Hu, Y. Zheng, L. Zheng, J. Mao, H. Liu, X. W. Du, M. Jaroniec, S. Z. Qiao, *Nat. Commun.* **2017**, *8*, 1509.
- [37] J. Durst, A. Siebel, C. Simon, F. Hasché, J. Herranz, H. A. Gasteiger, *Energ. Environ. Sci.* **2014**, *7*, 2255.
- [38] K. Li, Y. Li, Y. Wang, J. Ge, C. Liu, W. Xing, *Energ. Environ. Sci.* **2018**, *11*, 1232.
- [39] J. Wang, F. Xu, H. Jin, Y. Chen, Y. Wang, Adv. Mater. 2017, 29, 1605838.
- [40] G. Chen, T. Wang, J. Zhang, P. Liu, H. Sun, X. Zhuang, M. Chen, X. Feng, *Adv. Mater.* **2018**, *30*, 1706279.
- [41] L. Zhang, Y. Jia, H. Liu, L. Zhuang, X. Yan, C. Lang, X. Wang, D. Yang, K. Huang, S. Feng, X. Yao, *Angew. Chem. Int. Ed.* **2019**, *58*, 9404.
- [42] Z. Pu, I. S. Amiinu, Z. Kou, W. Li, S. Mu, Angew. Chem. Int. Ed. 2017, 56, 11559.
- [43] J. N. Tiwari, N. K. Dang, S. Sultan, P. Thangavel, H. Y. Jeong, K. S. Kim, *Nat. Sustain.* **2020**, 3, 556.

- [44] A. M. Harzandi, S. Shadman, M. Ha, C. W. Myung, D. Y. Kim, H. J. Park, S. Sultan, W.-S. Noh, W. Lee, P. Thangavel, W. J. Byun, S.-h. Lee, J. N. Tiwari, T. J. Shin, J.-H. Park, Z. Lee, J. S. Lee, K. S. Kim, *Appl. Catal. B* **2020**, 270, 118896.
- [45] L. Ma, L. R. L. Ting, V. Molinari, C. Giordano, B. S. Yeo, *J. Mater. Chem. A* **2015**, *3*, 8361.
- [46] A. B. Laursen, K. R. Patraju, M. J. Whitaker, M. Retuerto, T. Sarkar, N. Yao, K. V. Ramanujachary, M. Greenblatt, G. C. Dismukes, *Energ. Environ. Sci.* **2015**, *8*, 1027
- [47] J. R. McKone, B. F. Sadtler, C. A. Werlang, N. S. Lewis, H. B. Gray, *ACS Catal.* **2013**, *3*, 166.
- [48] Y. Zheng, Y. Jiao, A. Vasileff, S. Z. Qiao, Angew. Chem. Int. Ed. 2018, 57, 7568.
- [49] H. Tabassum, W. Guo, W. Meng, A. Mahmood, R. Zhao, Q. Wang, R. Zou, *Adv. Energy Mater.* **2017**, *7*, 1601671.
- [50] G. Kresse, J. Furthmuller, Phys. Rev. B 1996, 54, 11169.
- [51] J. P. Perdew, K. Burke, M. Ernzerhof, *Phys. Rev. lett.* **1996**, 77, 3865.
- [52] P. E. Blochl, Phys. Rev. B 1994, 50, 17953.
- [53] H. Xu, D. Cheng, D. Cao, X. C. Zeng, Nat. Catal. 2018, 1, 339.
- [54] S. Smidstrup, A. Pedersen, K. Stokbro, H. Jonsson, *J. Chem. Phys.* **2014**, *140*, 214106.

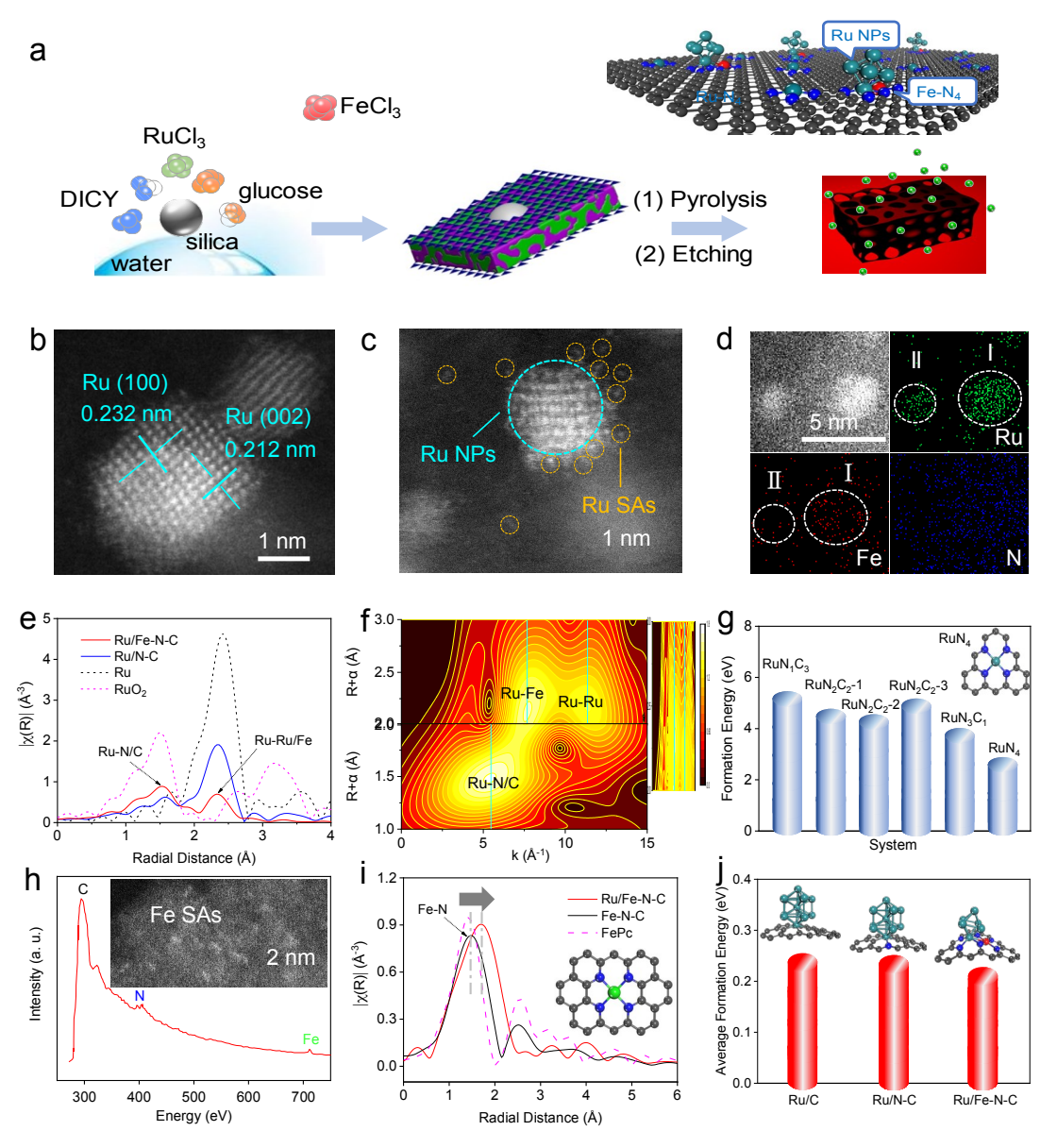


Figure 1. Morphology and structure of Ru/Fe-N-C. (a) Schematic procedures for the synthesis of Ru/Fe-N-C. (b) High-angle annular dark-field scanning TEM (HAADF-STEM) image of Ru NPs. (c) HAADF-STEM image implies the presence of Ru NPs and Ru SAs in Ru/Fe-N-C (Dashed aqua green circle indicates Ru NPs, while orange ones show the Ru SAs). (d) HAADF-STEM image and the corresponding elemental mapping of Ru, Fe and N. (e) Fourier transformed EXAFS k^3 -weighted $\chi(R)$ function spectra of Ru in Ru/Fe-N-C, Ru/N-C, Ru and RuO₂. (f) Wavelet transforms for the k^2 -weighted Ru K-edge EXAFS in Ru/Fe-N-C. (g) The calculated formation energy of RuN_xC_y (x+y≤4) structures in Ru/Fe-N-C. (h) Electron energy loss spectroscopic spectra (EELS) and corresponding HAADF-STEM image (inset) of Fe-N-C. (i) Fourier transformed EXAFS k^3 -weighted $\chi(R)$ function spectra of Fe in Fe-N-C, Ru/Fe-N-C and FePc. (j) The calculated average formation energy of three predicted structures (Ru/C, Ru/N-C and Ru/Fe-N-C).

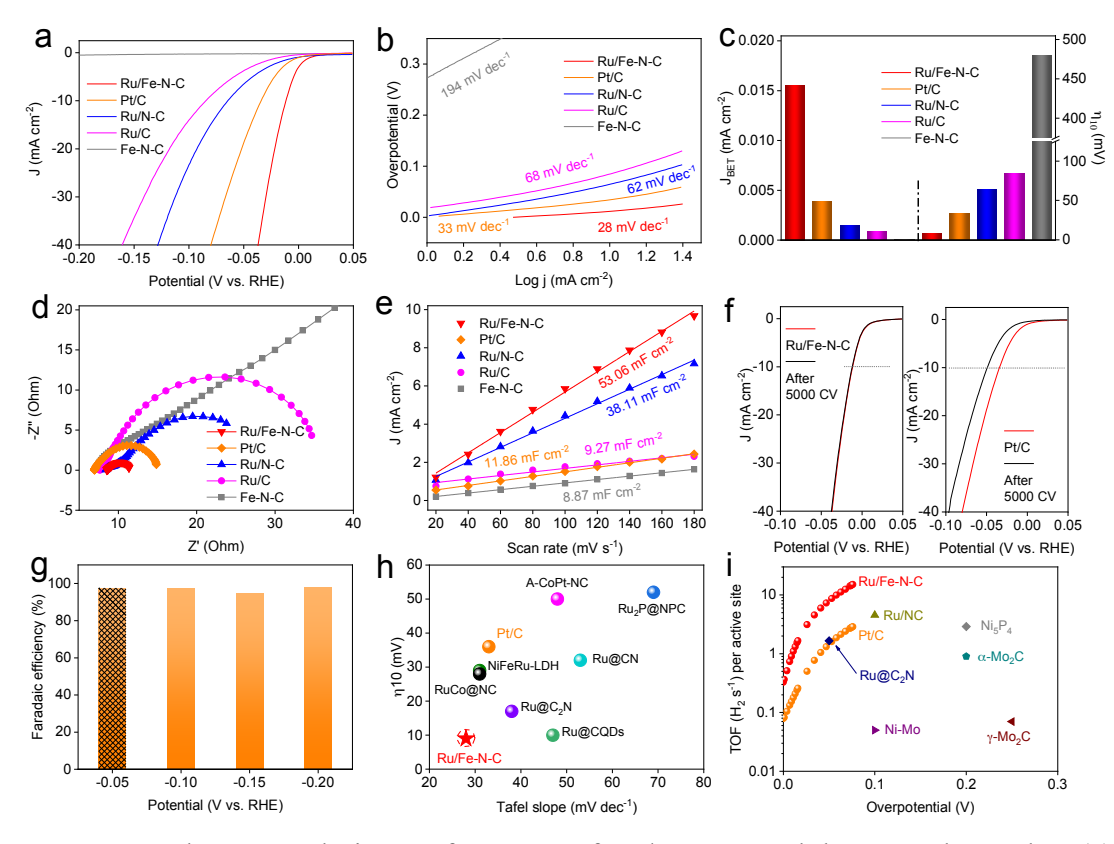


Figure 2. Hydrogen evolution performance of Ru/Fe-N-C and the control samples. (a) iR-corrected polarization curves with a scan rate of 2 mV s⁻¹ in 1 M KOH solution. (b) Tafel plots from the polarization curves. (c) The comparison of normalized current densities based on BET surface area at -0.05 V (vs. RHE) and overpotential at 10 mA cm⁻² (η_{10}). (d) The Nyquist plots at -0.1 V (vs. RHE). (e) the electrochemical double layer capacitance (C_{dl}) of Ru/Fe-N-C and other catalysts. (f) Durability test of Ru/Fe-N-C and Pt/C by recording the polarization curves before and after 5000 cycles. (g) Faradaic efficiency of Ru/Fe-N-C at different applied potentials. (h) The η_{10} versus Tafel slope of Ru/Fe-N-C in contrast to the reported catalysts. (i) TOF values of Ru/Fe-N-C compared with the reported catalysts.

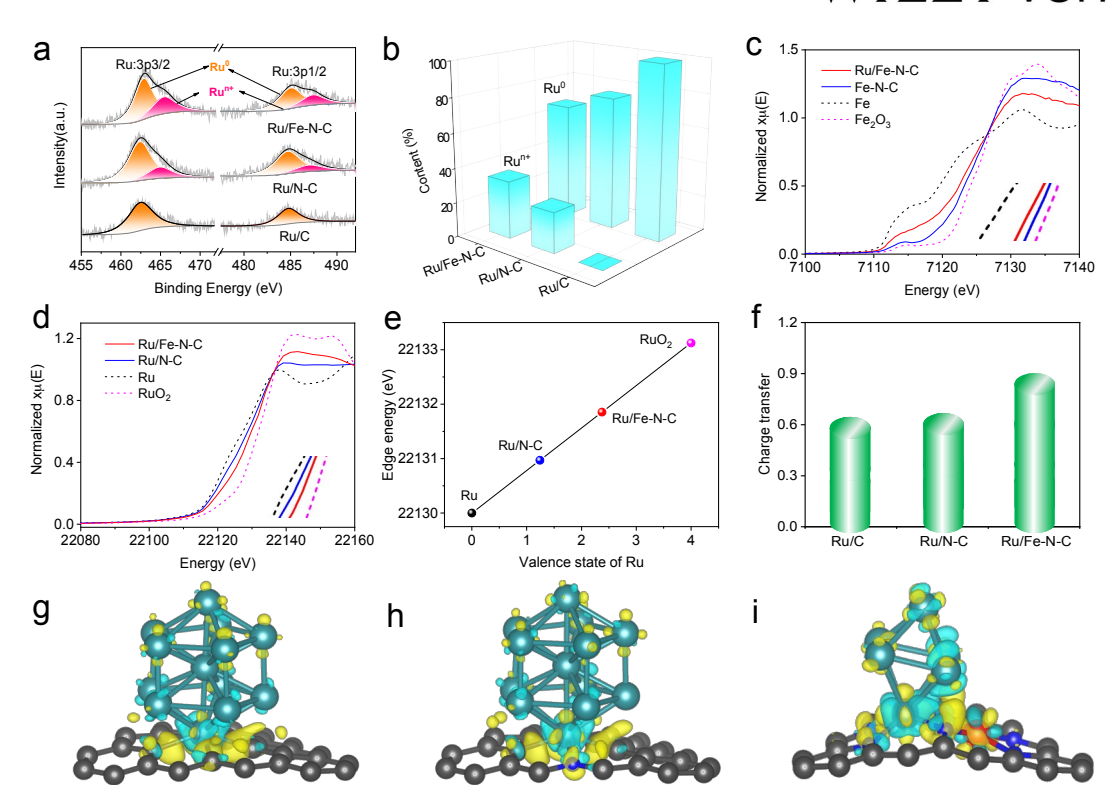


Figure 3. The interaction between Ru species and substrate in Ru/C, Ru/N-C and Ru/Fe-N-C. (a-b) High-resolution Ru 3p XPS spectra (a) and the corresponding Ru⁰ and Ruⁿ⁺ content (b) of Ru/Fe-N-C, Ru/N-C and Ru/C. (c) Fe K-edge XANES spectra of Fe-N-C, Ru/Fe-N-C, Fe and Fe₂O₃. (d) Ru K-edge XANES spectra of Ru/Fe-N-C, Ru/N-C, Ru and RuO₂. (e) Valence state of Ru in Ru/Fe-N-C and Ru/N-C, calculated from XANES results. (f) The charge transfer between Ru nanoclusters and substrate in three calculated structures (Ru/C, Ru/N-C and Ru/Fe-N-C). (g-i) The charge-density differences of three predicted structures (Ru/C, Ru/N-C and Ru/Fe-N-C) by DFT calculation. Yellow and blue regions represent the accumulation of positive and negative charge, respectively.

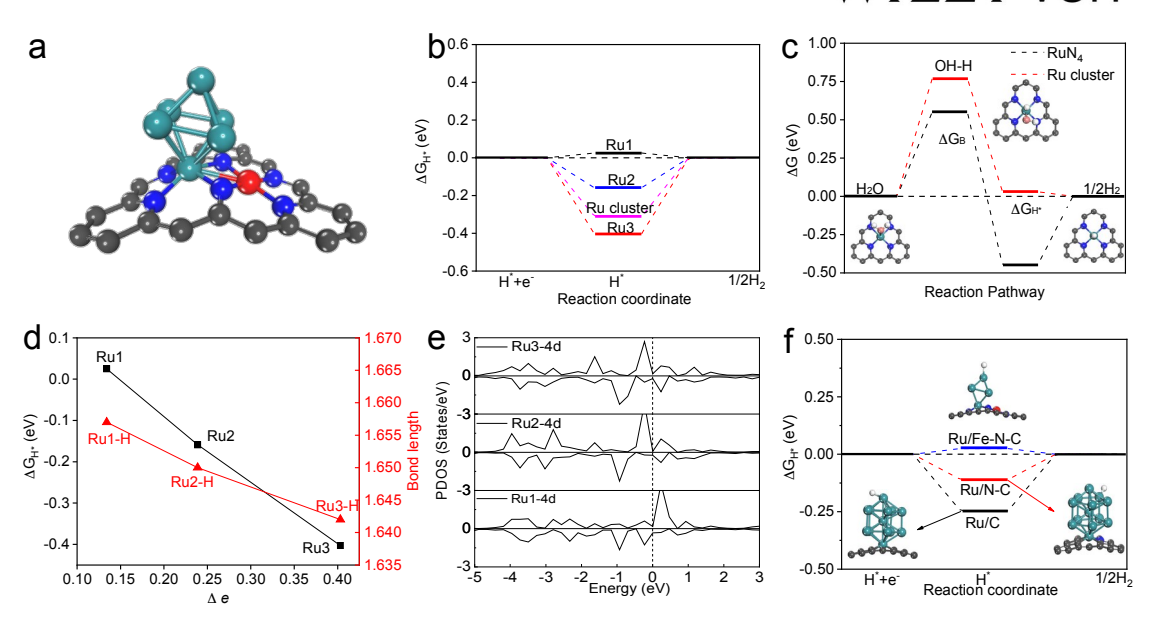


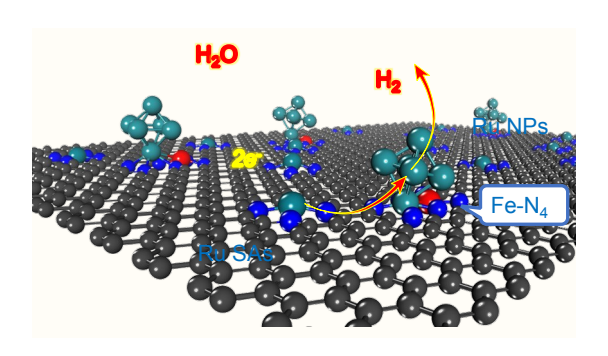
Figure 4. DFT calculations. (a) Atomic configurations of simulated Ru cluster with numbered Ru atoms in Ru/Fe-N-C system. (b) Hydrogen adsorption free energies (ΔG_{H^*}) of possible sites. The Ru1 site of interface between Ru cluster and Fe-N-C substrate exhibits high activity for HER. (c) Gibbs free energy diagram of HER on Ru-N₄ and Ru cluster in Ru/Fe-N-C system including reactant initial state, intermediate state, final state, and an additional transition state representing water dissociation. ΔG_B indicates water dissociation free energy barrier. (d) Correlation between and among ΔG_{H^*} , Ru-H bond length and charge transfer Δe^- of various Ru sites in simulated Ru/Fe-N-C with adsorbed H atom. (e) The projected density of state (pDOS) of various Ru sites of Ru cluster in Ru/Fe-N-C system. (f) Comparison of ΔG_{H^*} of HER on Ru/Fe-N-C, Ru/N-C, Ru/N-C system.

The table of contents entry: A nanocomposite of partial-single-atom and partial-nanoparticle formed within the Fe-N-C matrix serves as a multiple-site electrocatalyst toward hydrogen evolution reaction with an ultra-low overpotential of 9 mV to achieve 10 mA cm⁻², a high turnover frequency and ~100% Faradaic efficiency. Theoretical calculations reveal that ruthenium single-atom effectively facilitates water dissociation, and ruthenium nanoparticles promote hydrogen desorption.

Keyword: single-atom catalyst, multiple sites, electrocatalysis, water dissociation, theoretical calculation

Chun Hu, Erhong Song, Maoyu Wang, Wei Chen, Fuqiang Huang, Zhenxing Feng*, Jianjun Liu*, and Jiacheng Wang*

Partial-Single-Atom, Partial-Nanoparticle Composites Enhance Water Dissociation for Hydrogen Evolution



Supporting Information

Partial-Single-Atom, Partial-Nanoparticle Composites Enhance Water Dissociation for Hydrogen Evolution

Chun Hu, Erhong Song, Maoyu Wang, Wei Chen, Fuqiang Huang, Zhenxing Feng*, Jianjun Liu*, and Jiacheng Wang*

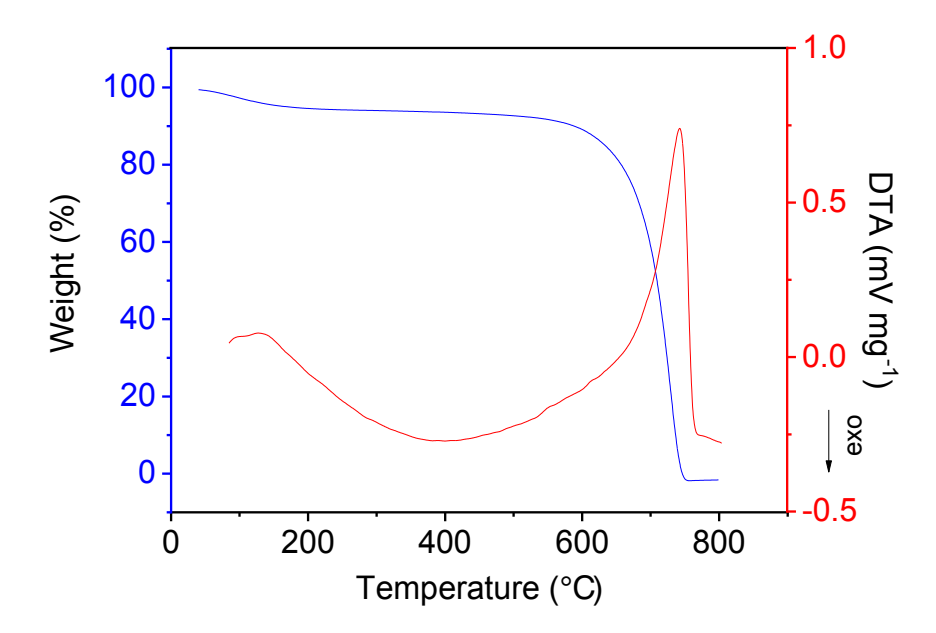


Figure S1 TG-DTA curves of pure g-C₃N₄ obtained in a nitrogen flow (10 °C/min). Pristine g-C₃N₄ shows 100% weight loss at 750 °C in a nitrogen flow with a ramp of 10 °C/min, implying its complete decomposition.

Ru/Fe-N-C sample was prepared from glucose, dicyanamide, FeCl₃, RuCl₃, and colloidal silica *via* pyrolysis and calcination (details in the experimental section). During pyrolysis, the as-formed layered graphitic carbon nitride (g-C₃N₄) composed of repeated melem building units could act as nitrogen source and confined nanospace for the formation of single-atom Fe-N₄ sites, that could *in-situ* intergrate with resulting Ru NPs. And the redundant g-C₃N₄ was naturally decomposed at increased pyrolysis temperature of 800 °C (Figure S1). Additionally, it is noteworthy that the presence of mesopores makes the maximized utilization of Fe-N₄ moieties by means of forming channels to the buried sites.^[1] The subsequent etching treatment by alkaline and acid solutions removed silica template and unstable Fe-related NPs to

obtain black Ru/Fe-N-C. During the calcination, Fe atom tends to coordinate with N species, obtaining Fe-N₄ moieties. Moreover, the layered texture of g-C₃N₄ and strong achoring ability of electronegative N atoms are able to avoid the overgrowth of Ru NPs.

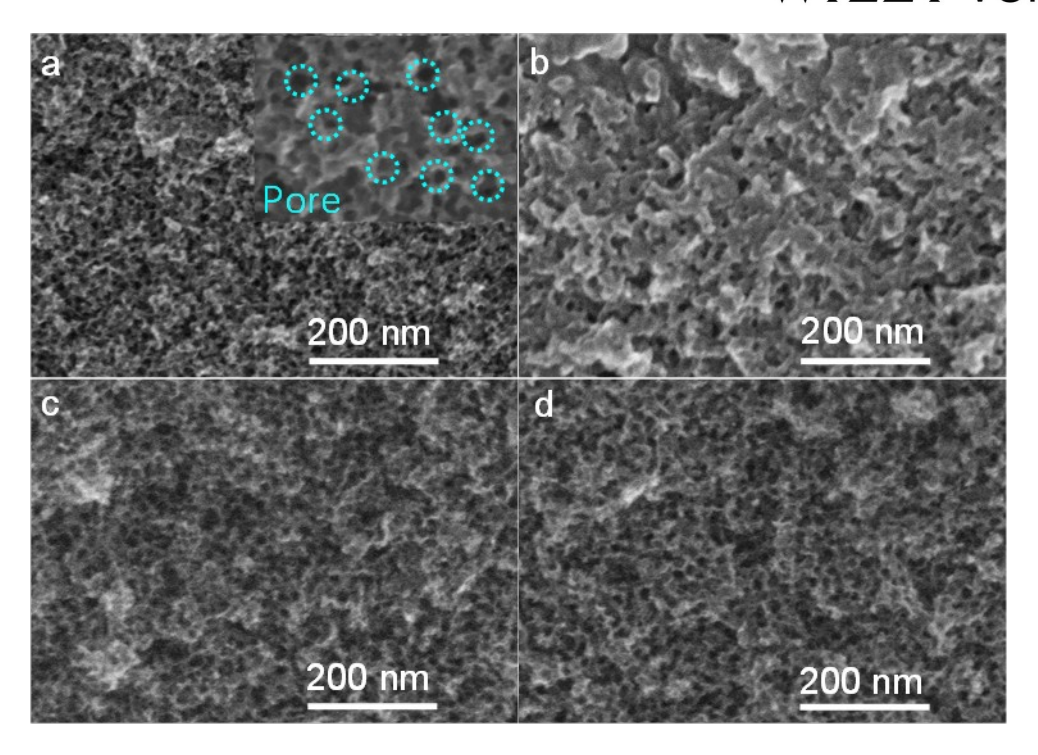


Figure S2 The scanning electron microscope (SEM) images of Ru/Fe-N-C, Fe-N-C, Ru/N-C and Ru/C.

The scanning electron microscopy (SEM) images shows that Ru/Fe-N-C, Fe-N-C, Ru/N-C and Ru/C possess uniform porous textures with abundant voids originated from residual room after removing silica (Figure S2). Well-defined porosity could increase the exposure of the accessible catalytic sites, thus improving the activity.

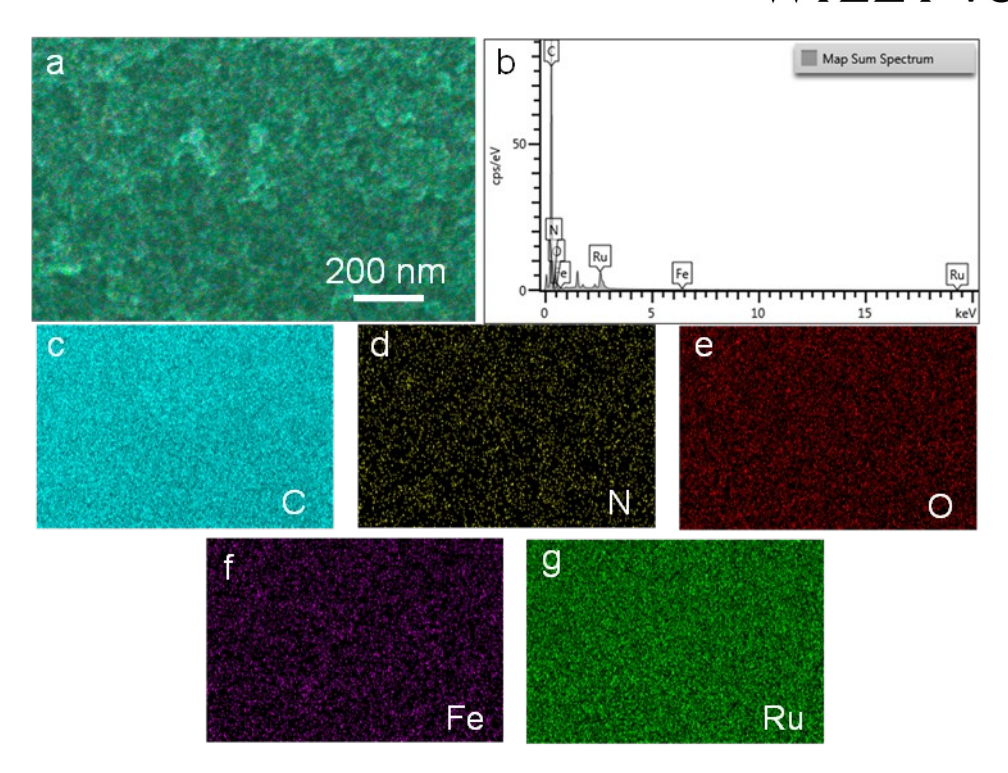


Figure S3 (a) Low magnification SEM image with the corresponding elemental mapping images of C (c), N (d), O (e), Fe (f) and Ru (g) for Ru/Fe-N-C. The resulting Ru/Fe-N-C consists of C, N, Fe, and Ru elements, as well as small amount of O element derived from trapped moisture and/or edged oxygen-containing groups.

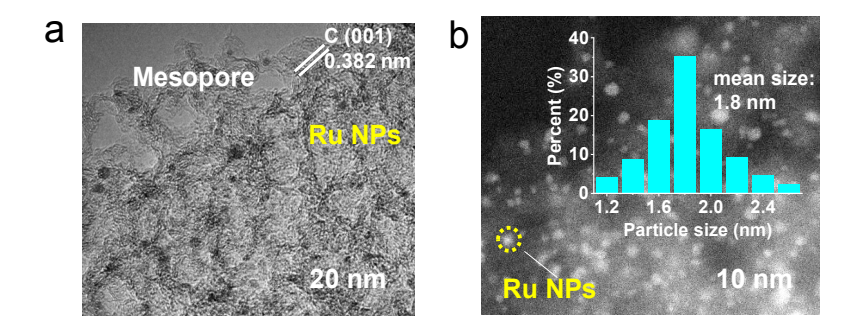


Figure S4 (a) Transmission electron microscopy (TEM) of Ru/Fe-N-C (Dashed yellow circles indicate Ru NPs, while white ones show the mesopores derived from residual room by etching off silica NPs) and high-resolution TEM (HRTEM) (inset). (b) High-angle annular dark-field scanning TEM (HAADF-STEM) image (inset: particle-size distribution of Ru NPs).

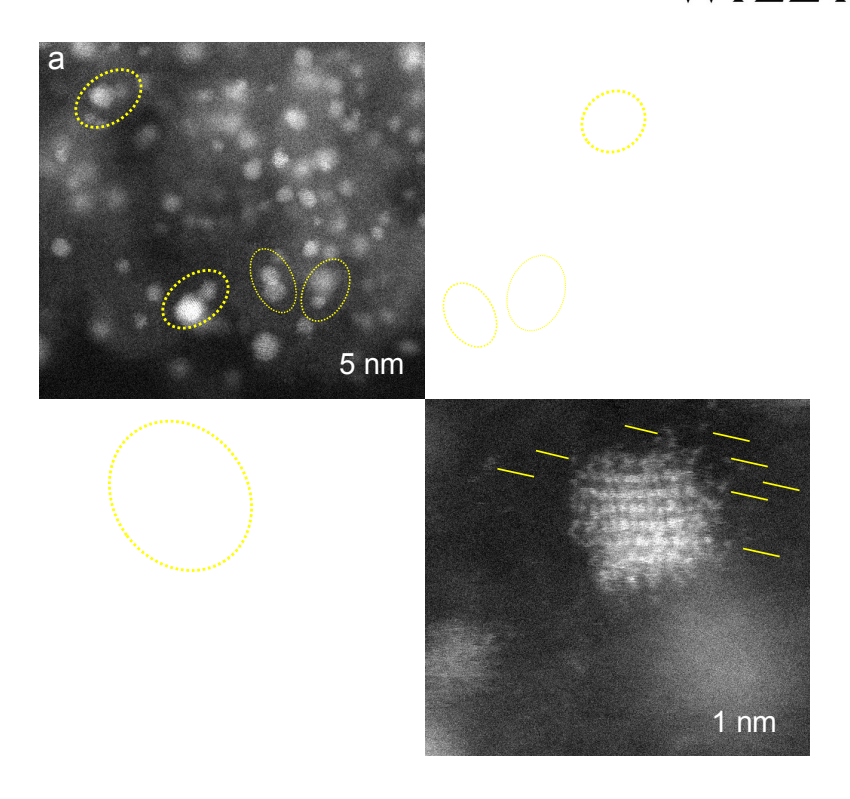


Figure S5 The High-angle annular dark-field scanning TEM (HAADF-STEM) images of Ru/Fe-N-C, where the dashed yellow circles indicate the aggregation of nanoparticles, and the yellow arrows signify Ru single-atoms/nanoclusters.

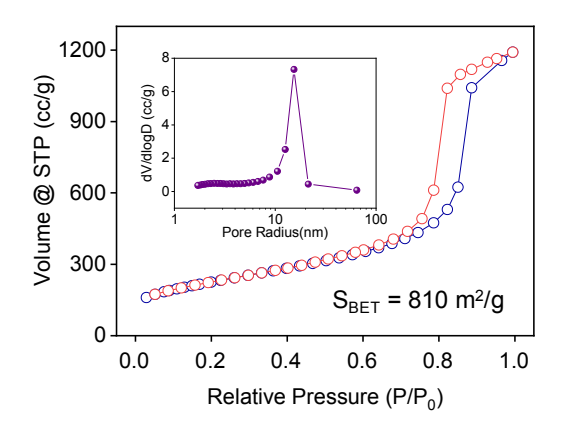


Figure S6 N_2 adsorption-desorption isotherms (inset: pore size distribution from the adsorption branch).

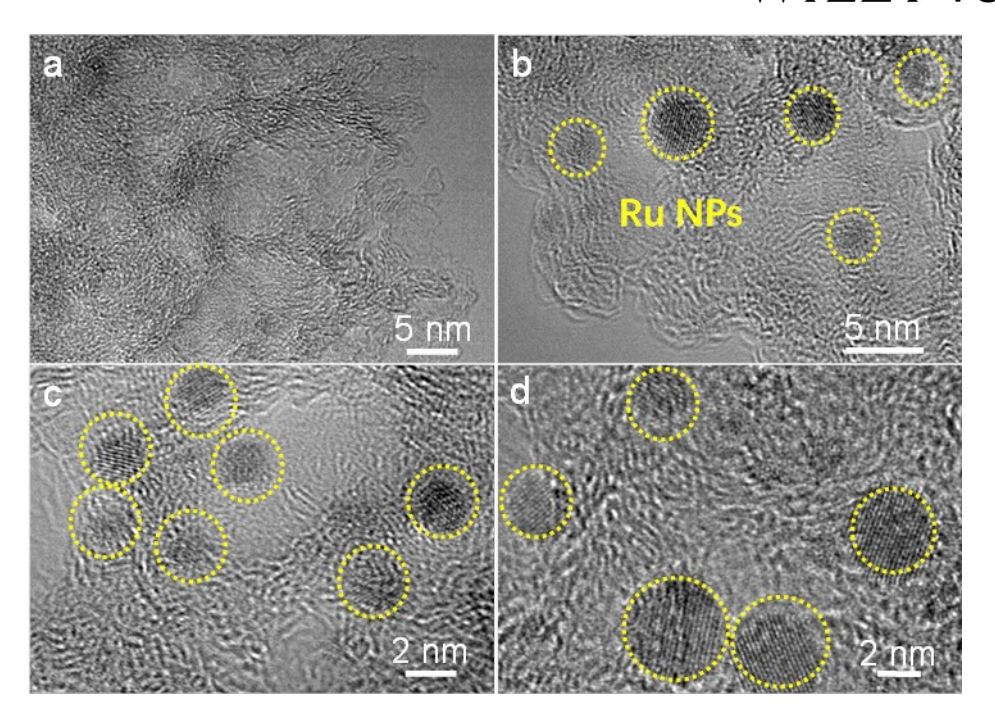


Figure S7 The high-resolution transmission electron microscopic (HRTEM) images of Fe-N-C, Ru0.05/Fe-N-C, Ru0.1/Fe-N-C, Ru0.3/Fe-N-C. With the increasing of Ru addition, the particle size of Ru tends to become larger.

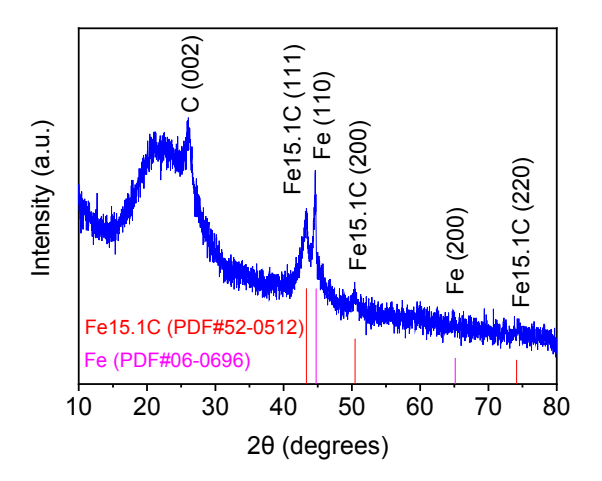


Figure S8 The XRD pattern of Ru/Fe-N-C before acid etching. It clearly indicates that Fe particles exist in the nanocomposite obtained by pyrolysis of glucose, dicyanamide, FeCl₃, and RuCl₃.

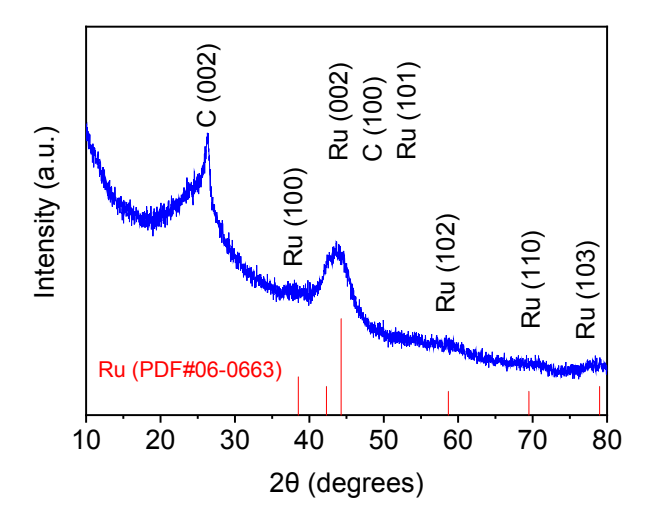


Figure S9 The X-ray diffraction (XRD) pattern of Ru/Fe-N-C.

The X-ray diffraction (XRD) pattern of Ru/Fe-N-C reveals well removal of Federived species after acid etching (Figure S8-9).

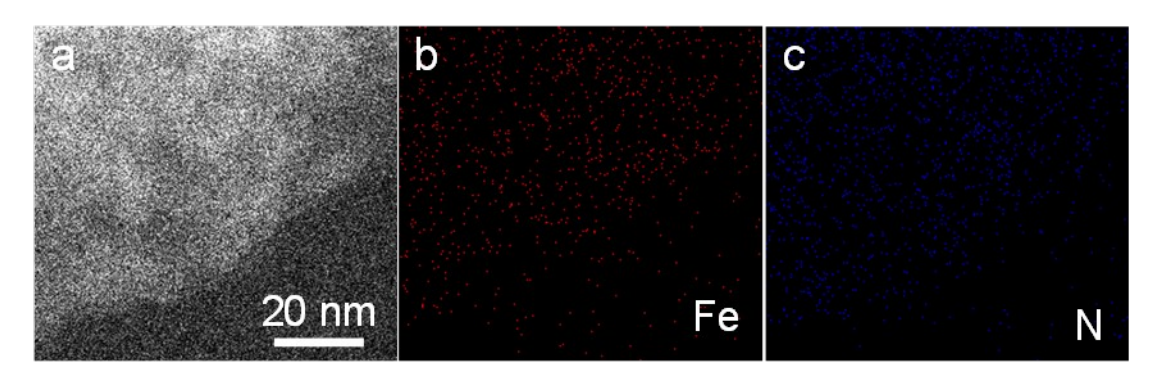


Figure S10 The high-angle annular dark-field scanning transmission electron microscopy (HAADF-STEM) of pristine Fe-N-C without Ru loading (a) and the corresponding elemental mappings of (b) Fe (red) and (c) N (blue). The Fe and N contents are 0.86 and 13.46 at%, respectively. No Fe nanoparticles could be observed, showing the high dispersion of Fe elements in the Fe-N-C sample.

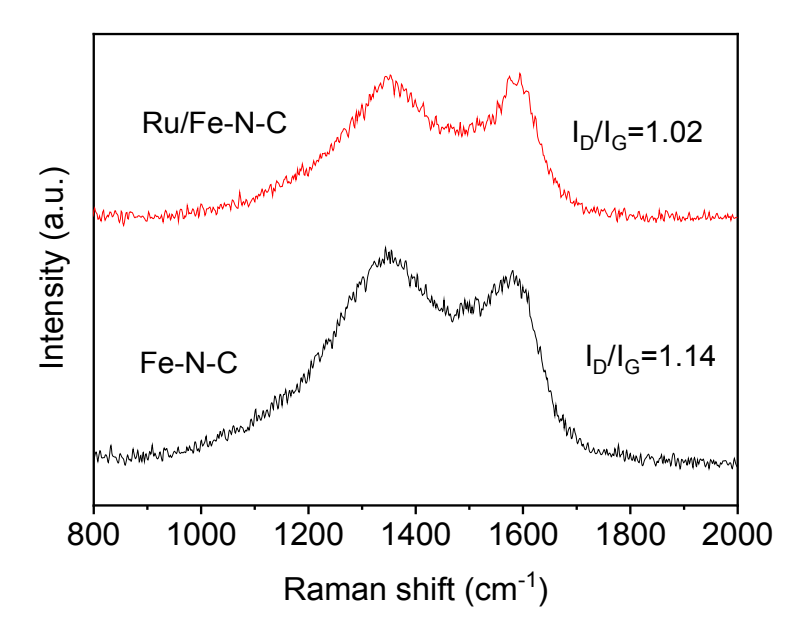


Figure S11 Raman spectra of Fe-N-C and Ru/Fe-N-C. A lower I_D/I_G for Ru/Fe-N-C value suggests the increased graphitization, which is advantageous for electron transport.

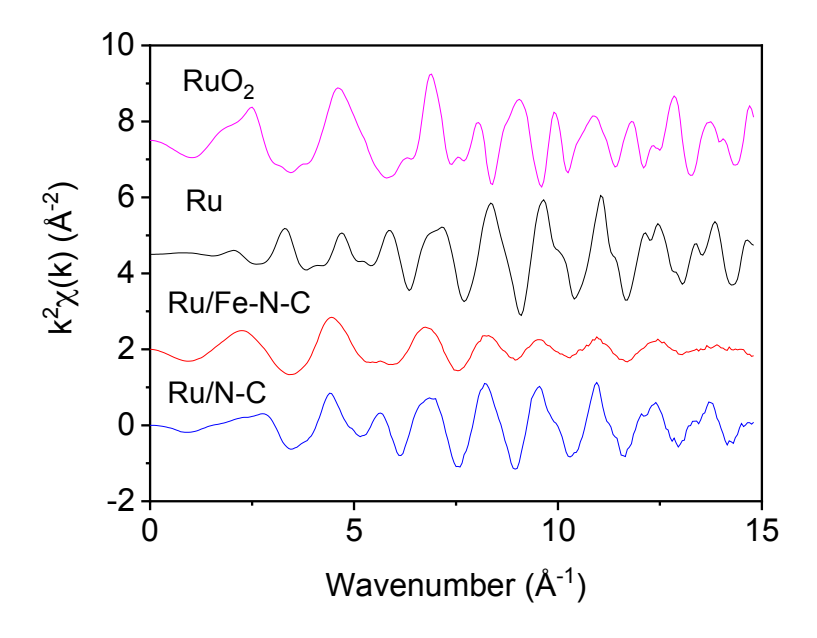


Figure S12 Ru K-edge EXAFS spectra of Ru/Fe-N-C, Ru/N-C, Ru and RuO₂ in k-space.

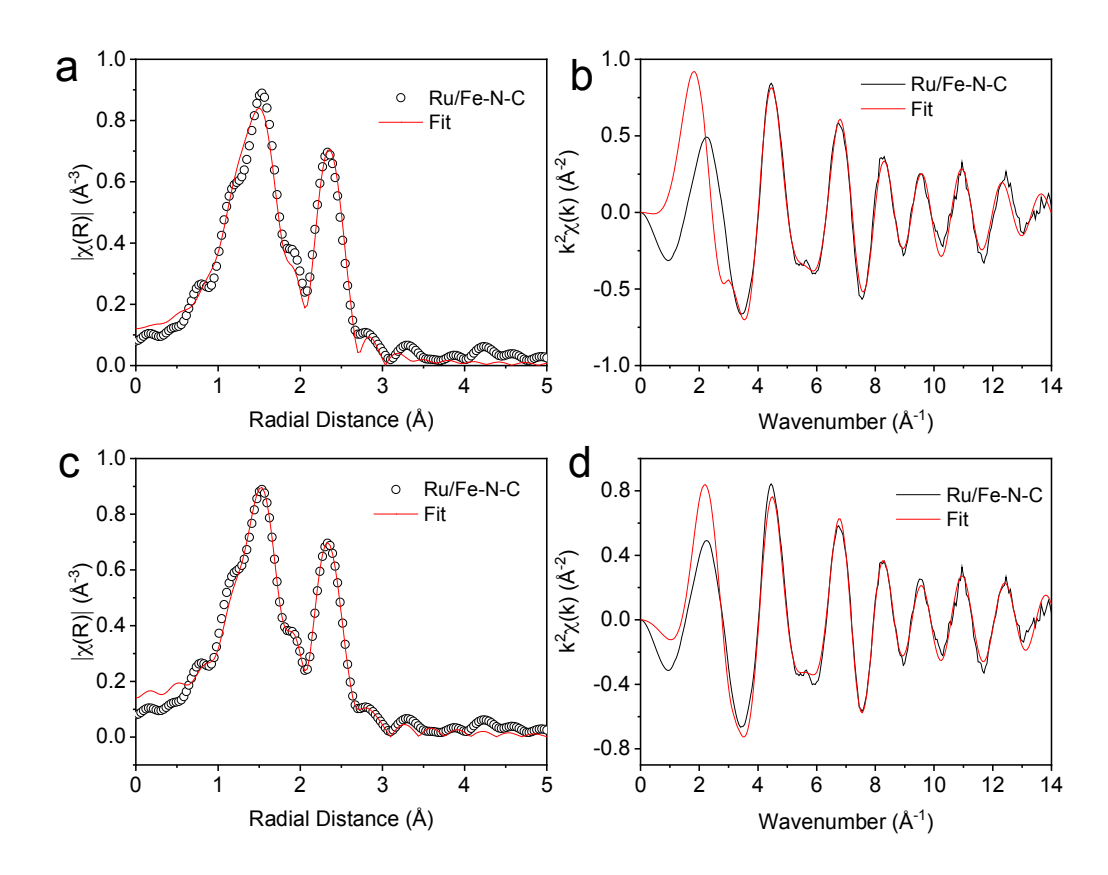


Figure S13 The EXAFS R-space fitting curve (red) and the experimental one (black cycles) of Ru/Fe-N-C (a) without Ru-Fe (c) with Ru-Fe. The EXAFS k-space fitting curve (red) and the experimental one (black) of Ru/Fe-N-C (b) without Ru-Fe (d) with Ru-Fe.

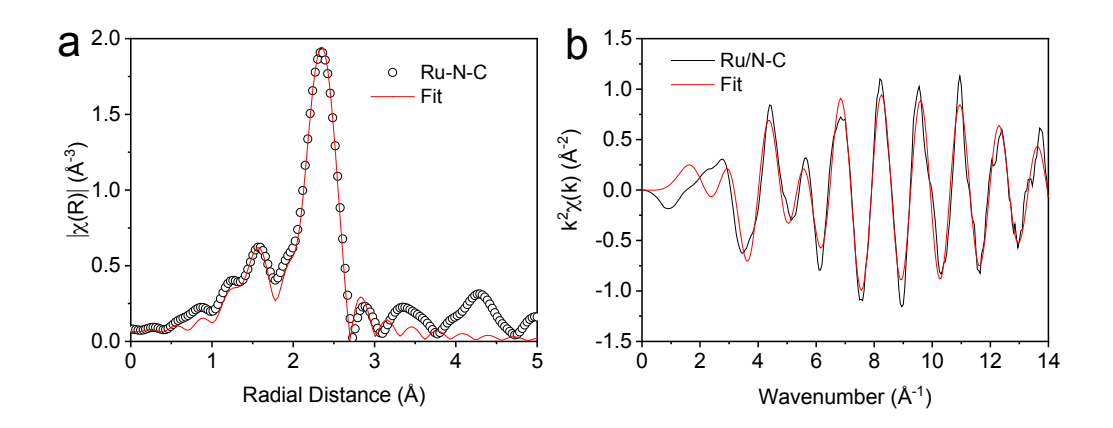


Figure S14 (a) The EXAFS R-space fitting curve (red) and the experimental one (black cycles) of Ru/N-C. (b) The EXAFS k-space fitting curve (red) and the experimental one (black) of Ru/N-C.

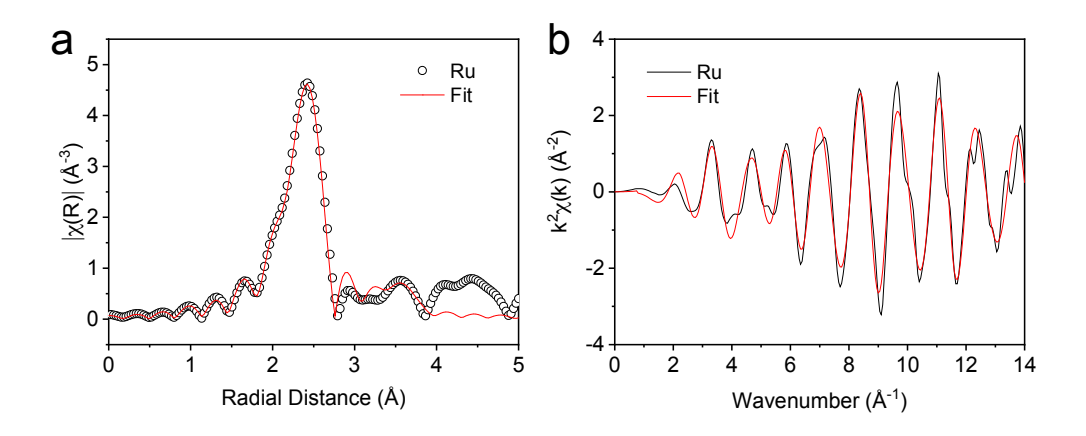


Figure S15 (a) The EXAFS R-space fitting curve (red) and the experimental one (black cycles) of Ru metal. (b) The EXAFS k-space fitting curve (red) and the experimental one (black) of Ru metal.

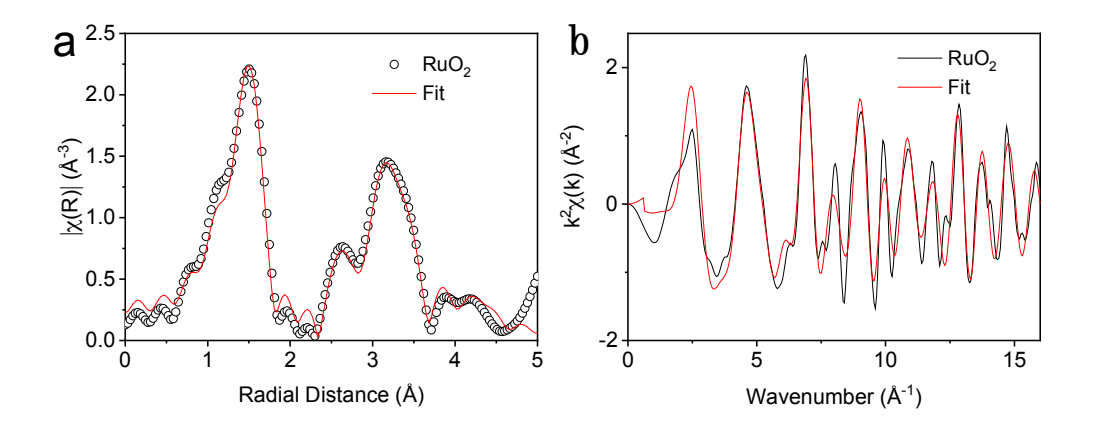


Figure S16 (a) The EXAFS R-space fitting curve (red) and the experimental one (black cycles) of RuO_2 . (b) The EXAFS k-space fitting curve (red) and the experimental one (black) of RuO_2 .

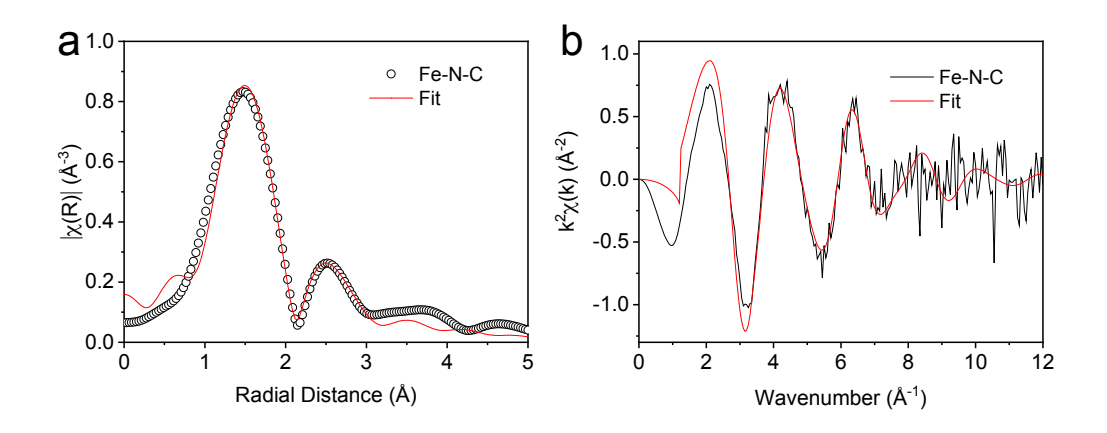


Figure S17 (a) The EXAFS R-space fitting curve (red) and the experimental one (black cycles) of Fe-N-C. (b) The EXAFS k-space fitting curve (red) and the experimental one (black) of Fe-N-C.

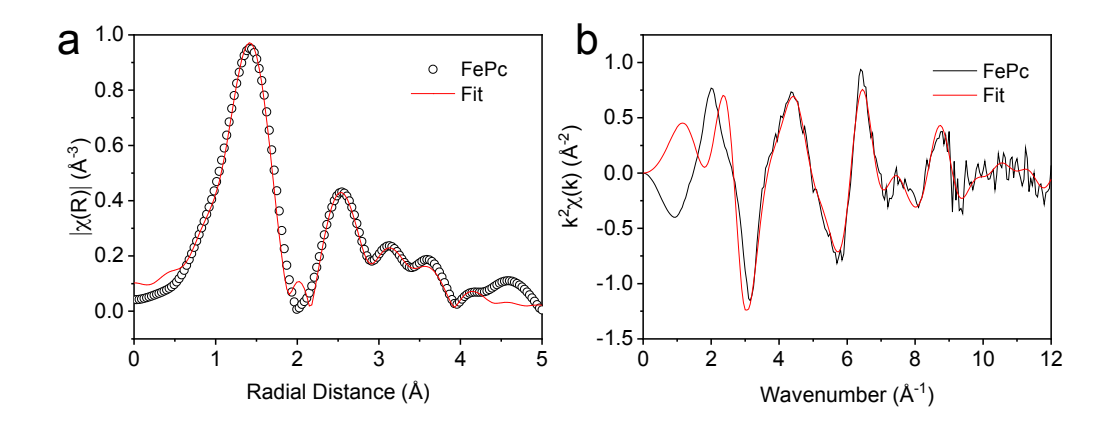


Figure S18 (a) The EXAFS R-space fitting curve (red) and the experimental one (black cycles) of FePc. (b) The EXAFS k-space fitting curve (red) and the experimental one (black) of FePc.

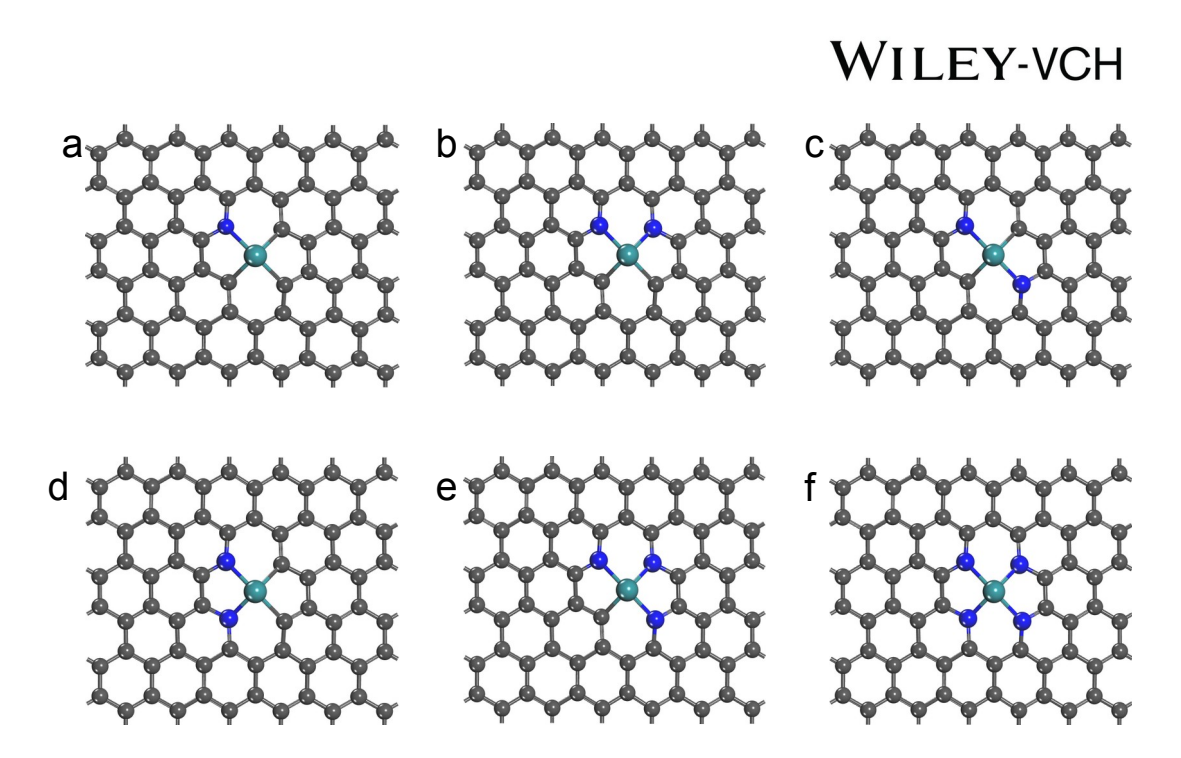


Figure S19 Atomic configurations of simulated RuN_1C_3 (a), RuN_2C_2 -1 (b), RuN_2C_2 -2 (c), RuN_2C_2 -3 (d), RuN_3C_1 (e) and RuN_4 (f).

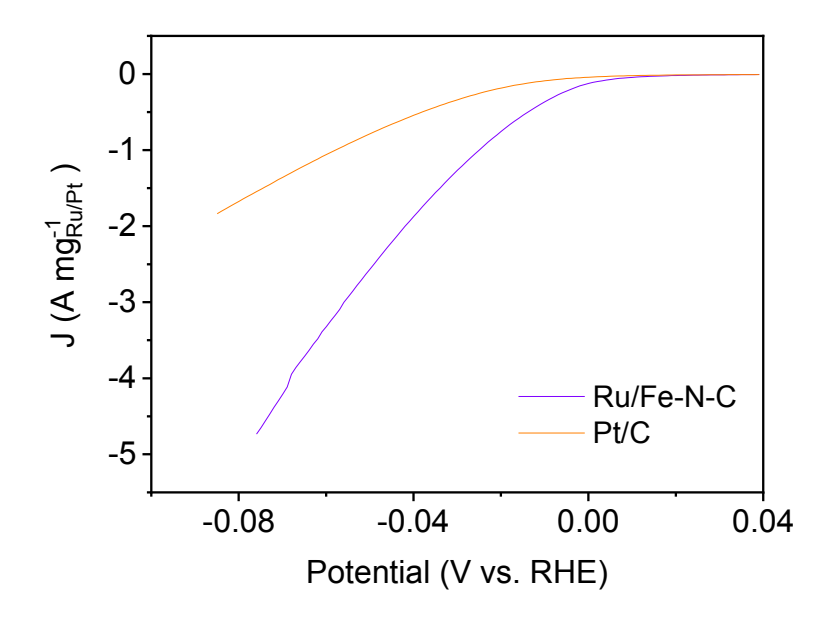


Figure S20 Mass activity of Ru/Fe-N-C and Pt/C.

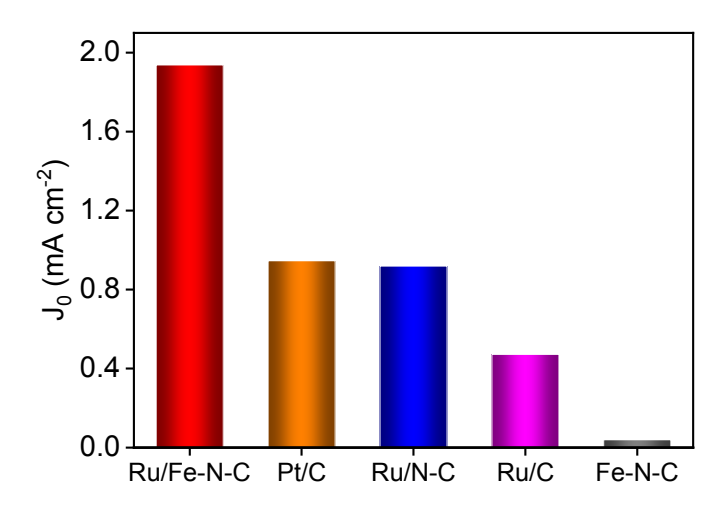


Figure S21 The exchange current density (J_0) of Ru/Fe-N-C, Pt/C, Ru/N-C, Ru/C and Fe-N-C.

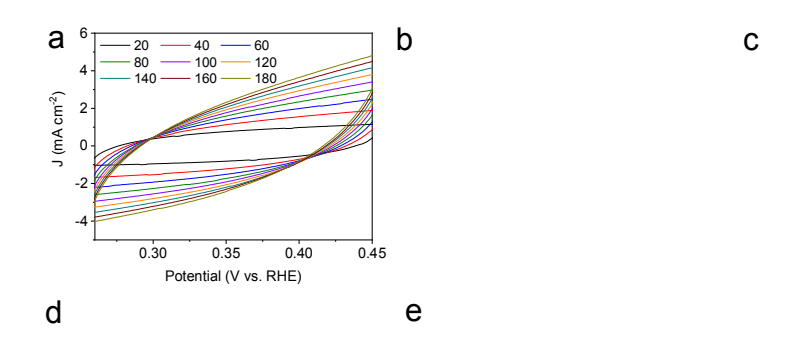


Figure S22 Cyclic Voltammetry curves of Fe-N-C (a), Ru/Fe-N-C (b), Ru/N-C (c), Ru/C (d) and commercial Pt/C (e) catalysts with various scan rates in 1M KOH solution. The capacitive currents were collected at 0.35 V vs. RHE in potential range where no Faradaic processes were present.

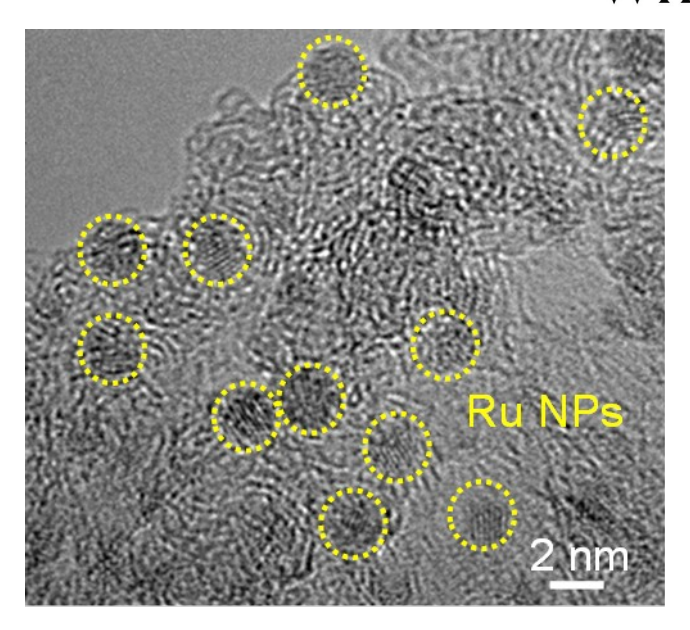


Figure S23 HRTEM image of Ru/Fe-N-C after 5000 CV.

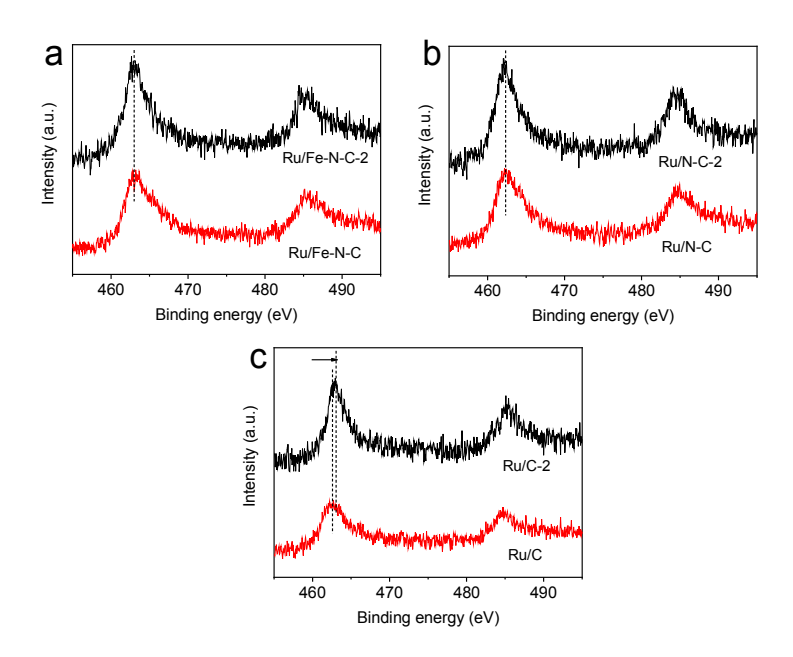


Figure S24. The Ru 3p XPS spectrum of Ru/Fe-N-C (a), Ru/N-C (b) and Ru/C (c) in their initial state and after long-term exposure to air.

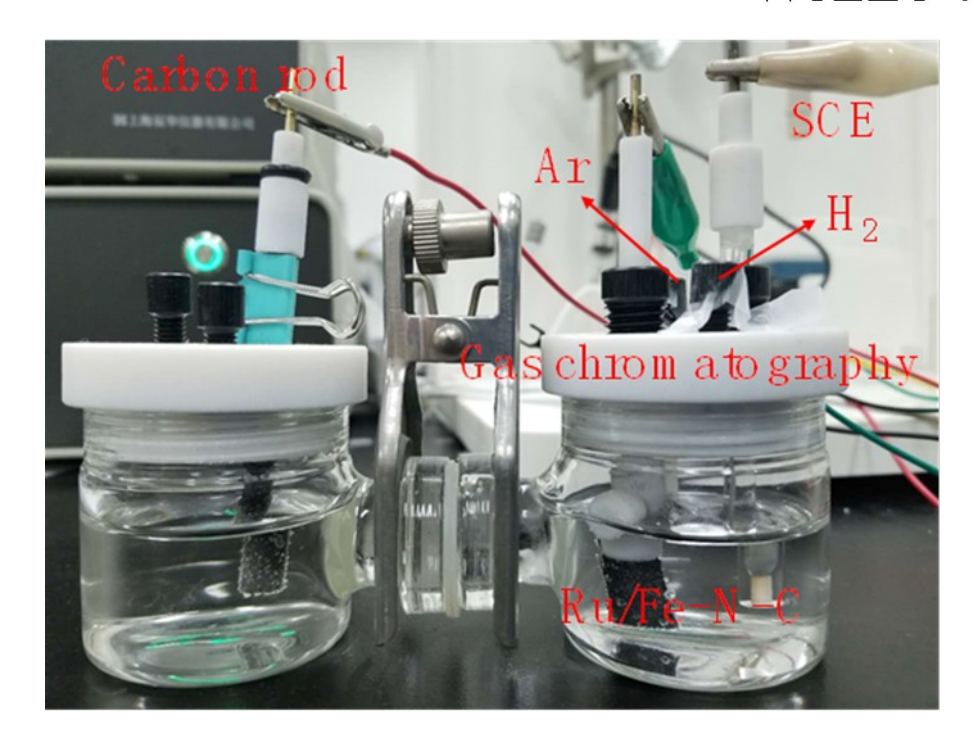


Figure S25 The details of hydrogen evolution Faradaic efficiency measurement in 1M KOH.

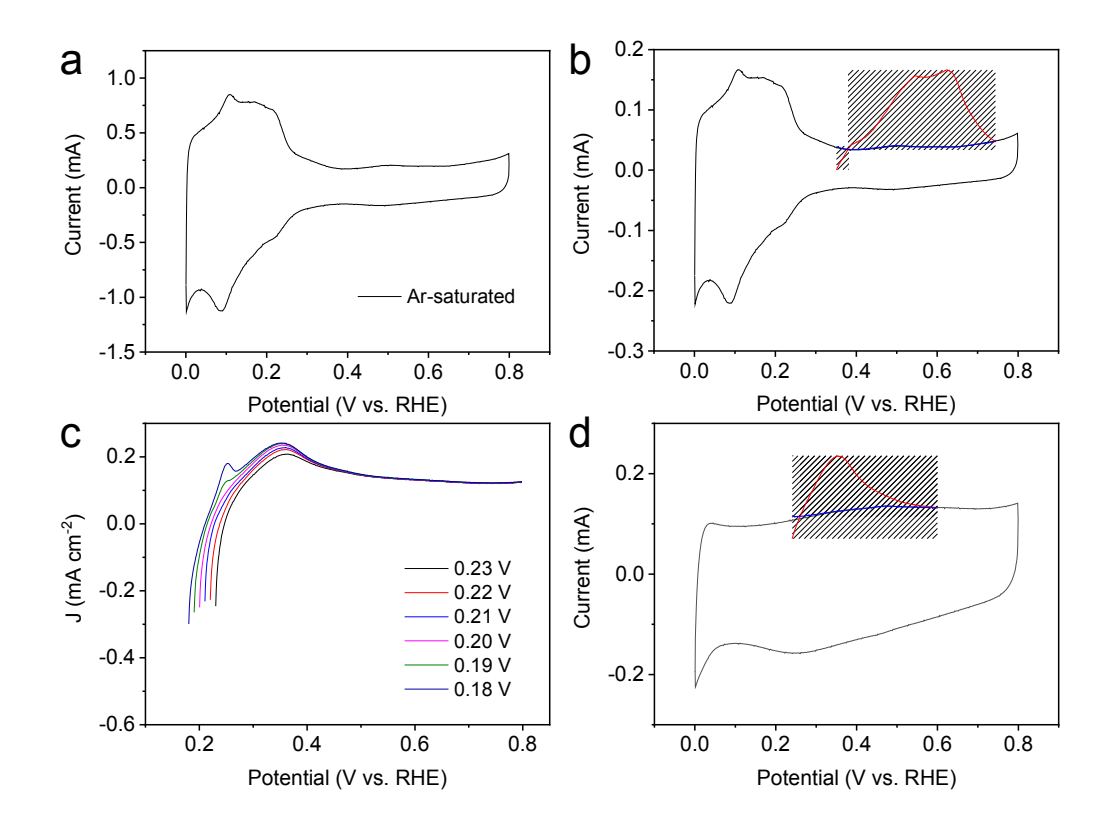


Figure S26 (a) Cycling voltammetry of Pt/C in 0.5 M H₂SO₄. (b) Cu UPD in 0.5 M H₂SO₄ in the absence (blue line) and presence (red line) of 5 mM CuSO₄ on Pt/C. The electrode was polarized at 0.205 V for 100 s to form the UPD layer. (c) Cu UPD in 0.5 M H₂SO₄ in the presence of 5 mM CuSO₄ on Ru/Fe-N-C. The electrode was polarized at 0.230, 0.220, 0.210, 0.200, 0.190 and 0.180 V for 100 s to form the UPD layers, respectively. (d) Cu UPD in 0.5 M H₂SO₄ in the absence (blue line) and presence (red line) of 5 mM CuSO₄ on Ru/Fe-N-C. The electrode was polarized at 0.200 V for 100 s to form the UPD layer. Scan rate: 10 mV s⁻¹.

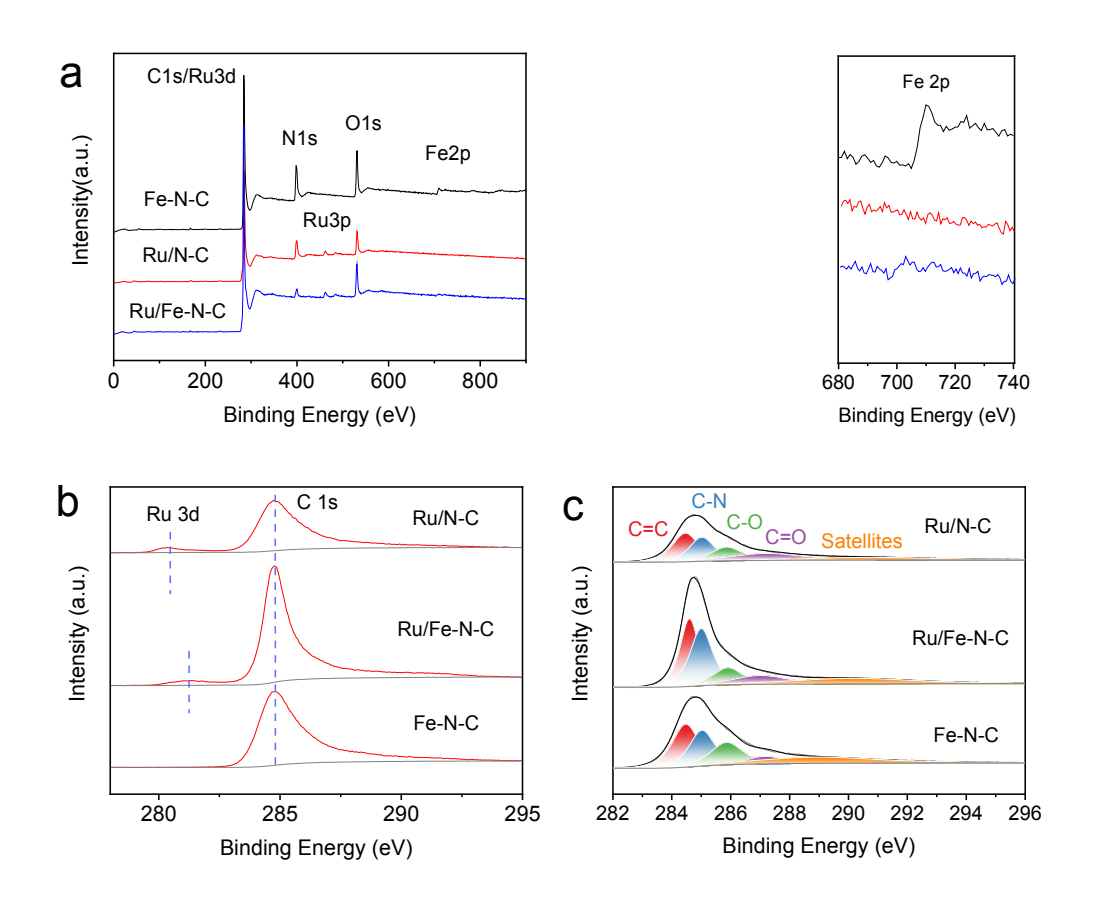


Figure S27 The XPS survey spectra (a), Ru 3d spectra (b) and C 1s spectra (c) of Ru/Fe-N-C, Ru/N-C and Fe-N-C.

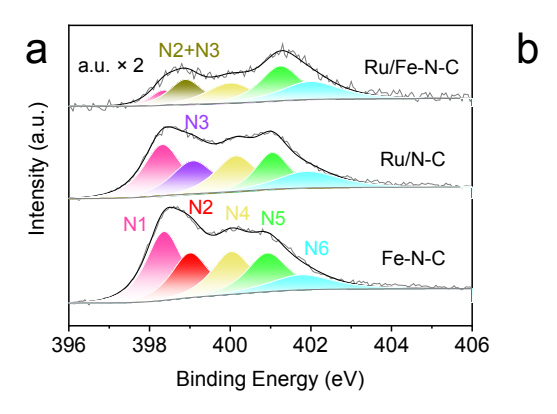


Figure S28 N1s XPS spectra (a) and corresponding N content of Ru/Fe-N-C, Ru/N-C and Fe-N-C (N1, N2, N3, N4, N5 and N6 are corresponding to pyrinidic N, Fe-N, Ru-N, pyrrolic N, graphitic N and N-oxides, respectively.).

N 1s spectrum of Ru/Fe-N-C displays pyridinic—N (398.2 eV), Ru/Fe-N bonding (398.9 eV), pyrrolic—N (400.1 eV), graphitic—N (401.2 eV), and oxidized—N (402.8 eV). Remarkably, the graphitic—N (~401.2 eV) becomes dominant in Ru/Fe-N-C compared to Fe-N-C, favorably improving the electronic conductivity of catalyst, and thus enhancing the HER activity

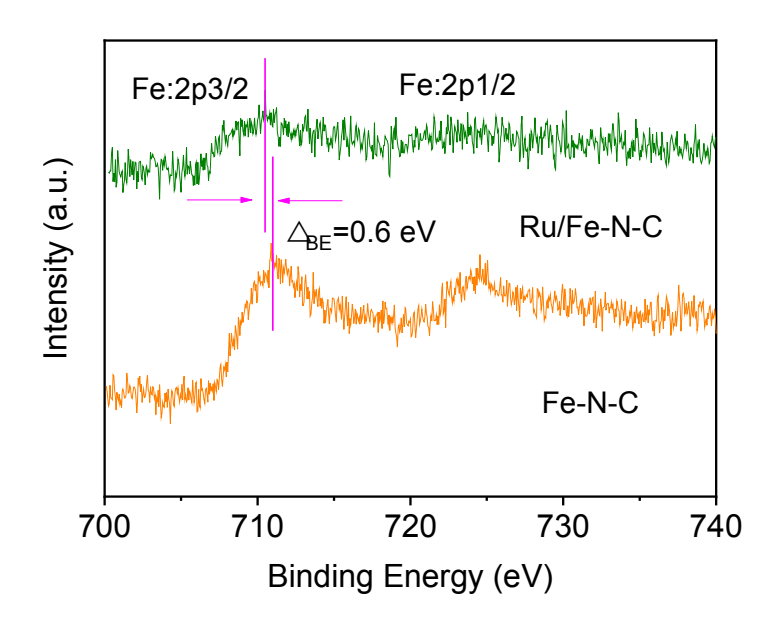


Figure S29 High-resolution Fe 2p XPS spectra of Ru/Fe-N-C and Fe-N-C.

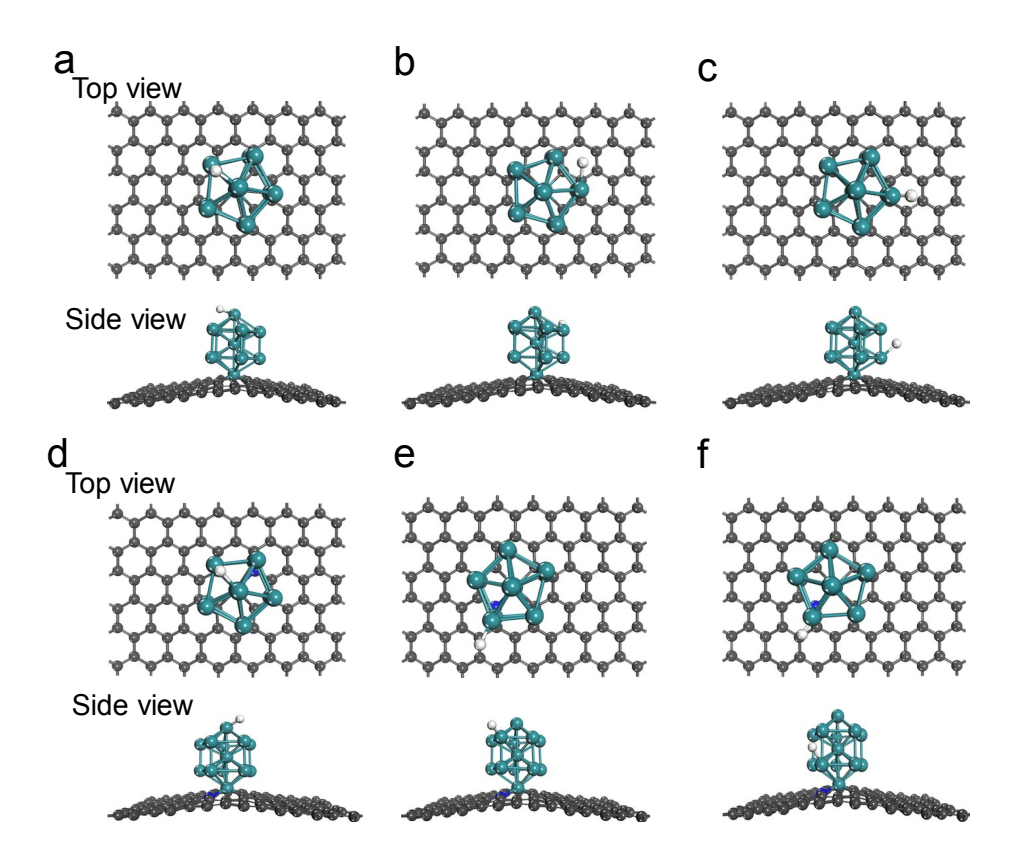


Figure S30 Optimized structure of H adsorbed on Ru1 (a), Ru2 (b) and Ru3 (c) atom of Ru/C system. And optimized structure of H adsorbed on Ru1 (d), Ru2 (e) and Ru3 (f) atom of Ru/N-C system.

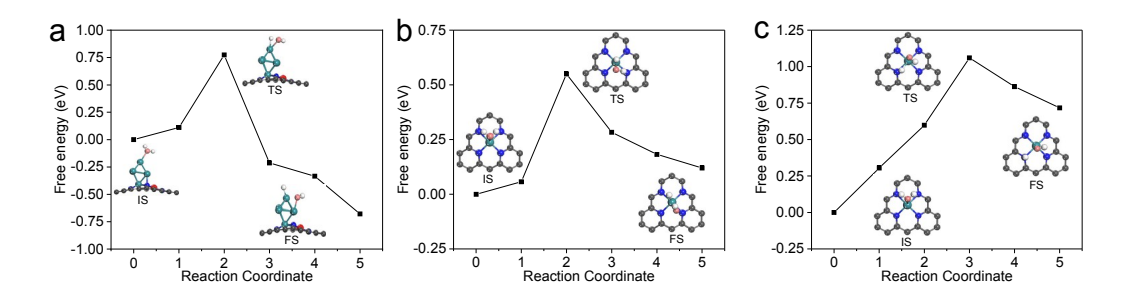


Figure S31 Water dissociation barrier of Ru cluster in Ru/Fe-N-C system (a). And water dissociation barrier for (b) reaction pathway-1 and (c) reaction pathway-2 of Ru-N₄ in Ru/Fe-N-C system. The insets are the structure of the corresponding transition state. The colors of elements are: gray for C, blue for N, red for Fe, pink for O and white for H.

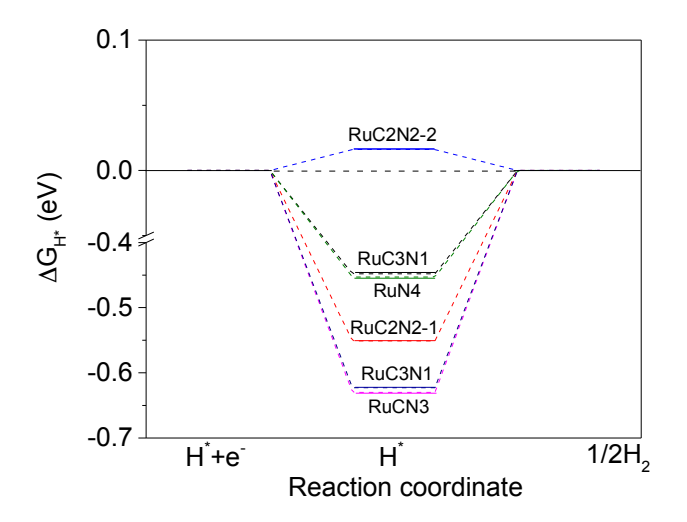


Figure S32 Calculated hydrogen adsorption free energy of multiple active site in Ru single atom system.

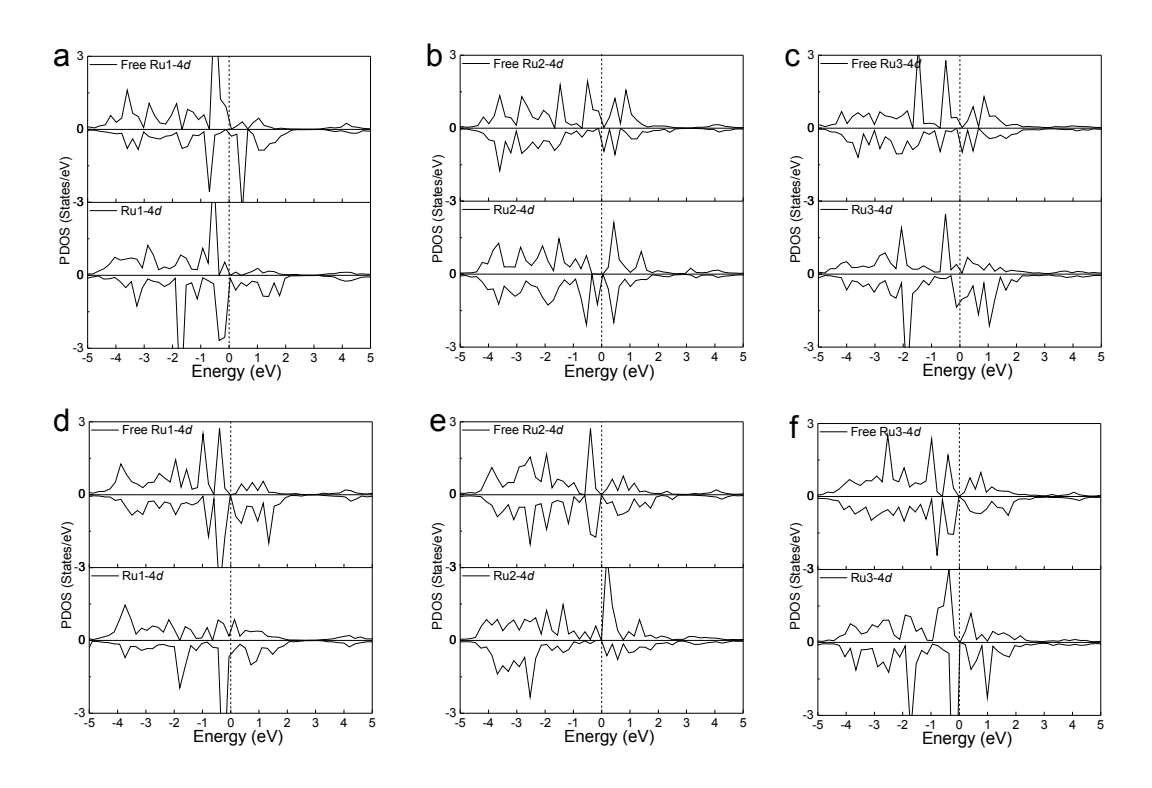


Figure S33 The projected density of state (pDOS) before and after H absorbed on Ru1 (a), Ru2 (b) and Ru3 (c) atom of Ru/C system. And the projected density of state (pDOS) before and after H absorbed on Ru1 (d), Ru2 (e) and Ru3 (f) atom of Ru/N-C system.

Table S1. Element contents for Ru/Fe-N-C determined by above EDS analysis.

Element	Line Type	Apparent Concentration	K Ratio	Wt. %
С	K series	11.77	0.11767	80.9
N	K series	0.12	0.00021	1.6
0	K series	0.31	0.00103	4.2
Fe	K series	0.21	0.00209	1.7
Ru	K series	1.41	0.01409	11.5
Total	K series	-	-	100.00

Table S2 Structural properties of the representative catalysts.

aatalyat	BET surface area	Pore size	Pore volume
catalyst	$(\mathbf{m}^2 \mathbf{g}^{-1})$	(nm)	$(\mathbf{m}^3 \mathbf{g}^{-1})$
Fe-N-C	840	8.7	1.8
Ru/Fe-N-C	810	9.3	1.8
Ru/N-C	880	10	2.1
Ru/ C	894	9.6	2.0

Table S3 Structure parameters (CN: coordination number; R: distance; σ^2 : mean-square disorder; $\triangle E_0$: energy shift) of Ru/Fe-N-C, Ru/N-C, RuO₂, bulk Ru metal, Fe-N-C, and standard FePc extracted from the EXAFS fitting. The single digit numbers in parentheses are the last digit errors. The numbers in parentheses for CN are the full errors.

Sample	Path	CN	R(Å)	$\sigma^2(\mathring{A}^2)$	${ m S_0}^2$	△E ₀ (eV)	R-factor
	Ru-N	6.4 ± 1.1	2.02 ± 0.01	0.0119(4)	1.9(3)		
Ru/Fe-N-C (without	Ru-Ru	1.8 ± 0.7	2.66 ± 0.03	0.0046(3)	0.22(3)	-4.9(5)	0.0227
Fe)	Ru-Ru	1.8 ± 0.7	2.72 ± 0.03	0.0099(7)	0.22(3)	1.5(0)	0.0227
	Ru-C	12.7 ± 2.3	3.07 ± 0.04	0.0269(9)	1.9(3)		
	Ru-N	3.8 ± 0.3	2.03 ± 0.01	0.0076(9)	1.1(1)		
	Ru-Fe	1± 0	2.60 ± 0.02	0.0200(7)	1.1(1)		
Ru/Fe-N-C (with Fe)	Ru-Ru	1.8 ± 0.3	2.65 ± 0.01	0.0033(5)	0.2(3)	-0.9(1)	0.0070
	Ru-Ru	1.8 ± 0.3	2.76 ± 0.02	0.0062(8)	0.2(3)		
	Ru-C	1.8 ± 0.3	2.89 ± 0.03	0.0080(4)	1.1(2)		
Ru/N-C	Ru-N	1.2 ± 0.2	2.00 ± 0.03	0.0033(8)	0.37(5)	-6.6(6)	0.0128

		3.9 ±	2.64 ±				
	Ru-Ru	0.01	0.02	0.0063(1)	0.45(1)		
	Ru-Ru	3.9 ±	2.70 ±	0.0035(2)	0.45(1)		
	Nu-Nu	0.01	0.02	0.0033(2)	0.43(1)		
	Fe-N	4	2.03 ±	0.0096(9)			
	1.6-11	4	0.02	0.0090(9)			
Fe-N-C	Fe-C	8	3.06 ±	0.0150(2)	1.3(1)	5.5(5)	0.0166
10-IN-C	10-0	0	0.04	0.0130(2)	1.5(1)	3.3(3)	0.0100
	Fe-N-C	16	3.28 ±	0.0136(1)			
	1.6-14-6	10	0.07	0.0130(1)			
	Fe-N	4	1.93 ±	0.0076(3)			
	1011	7	0.01	0.0070(3)			
	Fe-C	8	2.97 ±	0.0071(4)			
	100	O	0.02	0.0071(1)			
	Fe-N-C	16	3.14 ±	0.0029(2)			
	1010	10	0.02	0.0027(2)			
	Fe-N	4	3.37 ±	0.0057(5)			
FePc	1011		0.02	0.0007(0)	1.2(2)	-3.4(8)	0.0154
1 61 6	Fe-N-N	16	3.86 ±	0.0008(5)	1.2(2)	3.1(0)	0.0101
	101(1)	10	0.02	0.0000(5)			
	Fe-N-N	4	3.86 ±	0.0008(5)			
	101(1)		0.02	0.0000(5)			
	Fe-C	6	4.20 ±	0.0155(8)			
		Ÿ	0.03	0.0100(0)			
	Fe-N-C	12	4.22 ±	0.0093(1)			
			0.03	(1)			
Ru metal	Ru-Ru	6	2.64 ±	0.0026(9)	0.73(6)	2.4(9)	0.0164
			0.01				
	Ru-Ru	6	2.70 ±	0.0020(7)			

			0.01				
	Ru-Ru	6	3.77 ± 0.01	0.0038(2)			
	Ru-Ru-Ru	36	3.98 ± 0.01	0.0031(1)			
	Ru-O	2	1.95 ± 0.01	0.0010(4)			
	Ru-O	4	1.99 ± 0.01	0.0036(3)			
	Ru-Ru	2	3.12 ± 0.01	0.0024(4)			
	Ru-Ru	8	3.55 ± 0.01	0.0027(6)			
	Ru-O-Ru	16	3.74 ± 0.01	0.0024(5)			
RuO ₂ bulk	Ru-O	2	3.90 ± 0.01	0.0005(3)	0.94(9)	1.6(2)	0.0165
	Ru-O	4	3.98 ± 0.01	0.0007(2)			
	Ru-O-O	4	4.43 ± 0.01	0.0008(5)			
	Ru-Ru	4	4.51 ± 0.01	0.0037(2)			
	Ru-O	8	4.63 ± 0.01	0.0082(2)			
	Ru-O-O	16	4.70 ± 0.01	0.0341(1)			

Table S4 The calculated formation energy of RuN_xC_y (x+y \leq 4) structures in Ru/Fe-N-

C.

Structure	Formation energy
RuN ₁ C ₃	5.448
RuN_2C_2-1	4.75
RuN_2C_2 -2	4.519
RuN_2C_2-3	5.157
RuN_3C_1	3.985
RuN_4	2.871

 $\label{thm:calculated} \textbf{Table S5} \ \ \text{The calculated average formation energy and charge transfer between Rund nanoclusters and substrate of Ru/C, Ru/N-C and Ru/Fe-N-C structure.}$

Structure	Average formation energy	Charge
Ru/C	0.251	0.629

Ru/N-C	0.248	0.664
Ru/Fe-N-C	0.224	0.901

Table S6 Summary of some recently reported HER electrocatalysts in 1M KOH electrolyte.

Catalyst	Electrolyte	Overpotential	Tafel slope
	Electrolyte	at 10 mA cm ⁻² (mV)	(mV dec ⁻¹)
Ru/Fe-N-C	1M KOH	9	28
NiFeRu-LDH[2]	1M KOH	29	31

Cu NDs/Ni ₃ S ₂ NTs- CFs ^[3]	1M KOH	128	76.2
$NC/CuCo/CuCoO_x^{[4]}$	1M KOH	112	55
$EG/Co_{0.85}Se/$	1M KOH	260	160
NiFeLDH ^[5]	IWI KOTI	200	100
Se-(NiCo)S/OH ^[6]	1M KOH	101	87.3
$\mathbf{Ru}\mathbf{-MoO}_{2}^{[7]}$	1M KOH	29	31
Ni ₂ P NPs/CC ^[8]	1M KOH	71	73
$Ni@Ni_2P-Ru^{[9]}$	1M KOH	31	41
CoP/NCNHP ^[10]	1M KOH	115	66
$Ru_2P@NPC^{[11]}$	1M KOH	52	69
$\mathbf{NH_2\text{-}BP^{[12]}}$	1M KOH	290	63
NiCu@C ^[13]	1M KOH	74	94.5
$Ni_2P@NPCNFs^{[14]}$	1M KOH	104.2	79.7
$P-Co_3O_4^{[15]}$	1M KOH	120	52
$Mo_2N\!-\!Mo_2C/HGr^{[16]}$	1M KOH	154	68
Cu@NiFe LDH ^[17]	1M KOH	116	58.9
$\mathbf{Co\text{-}Ni_3N^{[18]}}$	1M KOH	194	156
$MoB/g-C_3N_4^{[19]}$	1M KOH	133	46
$\textbf{A-CoPt-NC}^{[20]}$	1M KOH	50	48
$NP\text{-}MoS_2/CC^{[21]}$	1M KOH	78	51.6
Co/b-Mo ₂ C@N- CNTs ^[22]	1М КОН	170	92
$Ru/NG-750^{[23]}$	1M KOH	8	30
$Ru@C_2N^{[24]}$	1M KOH	17	38
$RuCoP^{[25]}$	1M KOH	23	37
Co-substituted Ru ^[26]	1M KOH	13	29
[Ru(SA)			
+Ru(NP)@RuNx@GN	1M KOH	7	20
$]/GN^{[27]}$			

WILEY-VCH $Ru-NC-700^{[28]}$ 1M KOH 12 $Ru@CQDs^{[29]}\\$ 1M KOH 10 47 $RuCo@NC^{[30]}\\$ 1M KOH 28 31 $Ru@CN^{[31]}$ 1M KOH 32 53 RuSAs + 7 29 1M KOH $RuNPs@MHC^{[32]}\\$ $Cu/Ru@G_{N}^{[33]}$ 1M KOH 8 20 RuNi/CQDs^[34] 1M KOH 40 13 BPed-Pt/GR^[35] 1M KOH 46.9 21 $Ru@SC\text{-}CDs^{[36]}$ 1M KOH 29 57

Table S7 TOF values of Ru-based electrocatalysts in 1M KOH solution.

Catalyst	Electrolyte	TOF (H ₂ s ⁻¹)
Ru/Fe-N-C (This	1M KOH	3.6 at η=25 mV; 8.9 at η=50 mV
work)	IW KOII	3.0 at 1 23 m v, 0.7 at 1 30 m v
$Ru@C_2N^{[24]}$	1M KOH	0.76 at η =25 mV; 1.66 at η =50 mV
Ru/NC ^[37]	1M KOH	$4.55 \text{ at } \eta = 100 \text{ mV}$
$Ru/NG-750^{[23]}$	1M KOH	$0.35 \text{ at } \eta = 100 \text{ mV}$

RuCoP ^[25]	1M KOH	7.26 at η =100 mV
Co-substituted Ru ^[26]	1M KOH	2.15 at η =30 mV; 6.39 at η =60 mV
$Cu/Ru@G_N^{[33]}$	1M KOH	1.47 at η =20 mV
RuNi/CQDs ^[34]	1M KOH	$5.03 \text{ at } \eta = 100 \text{ mV}$
Ru@SC-CDs ^[36]	1M KOH	$0.56 \text{ at } \eta = 100 \text{ mV}$

Table $\bf S8$ Elemental composition of the representative catalysts from XPS.

Catalyst	Ru (wt. %)	Fe (wt. %)	N (wt. %)	C (wt. %)	O (wt. %)
Fe-N-C	0	3.7	14.5	70.4	11.4
Ru0.05/Fe-N-C	0.4	2.1	5.9	82.8	8.8
Ru0.1/Fe-N-C	0.89	1.96	4.7	79.95	12.5
Ru/Fe-N-C	1.42	1.98	3.67	84.03	8.9
Ru/N-C	2.88	0	12.7	74.51	9.91

Ru/C	2.62	0	0	81.77	15.61
Ru0.3/Fe-N-C	2.29	2.15	4.34	79.52	11.7

Table S9 Ru content of the catalysts from ICP-AES experiment.

Catalyst	Ru (wt. %)
Ru/Fe-N-C	4.92
Ru/N-C	8.06
Ru/C	8.47

- References for supporting information:
- [1] J. Pampel, T.-P. Fellinger, Adv. Energy Mater. 2016, 6, 1502389.
- [2] G. Chen, T. Wang, J. Zhang, P. Liu, H. Sun, X. Zhuang, M. Chen, X. Feng, *Adv. Mater.* **2018**, *30*, 1706279.
- [3] J. X. Feng, J. Q. Wu, Y. X. Tong, G. R. Li, J. Am. Chem. Soc. 2018, 140, 610.
- [4] J. Hou, Y. Sun, Y. Wu, S. Cao, L. Sun, Adv. Funct. Mater. 2018, 28, 1704447.
- [5] Y. Hou, M. R. Lohe, J. Zhang, S. Liu, X. Zhuang, X. Feng, *Energ. Environ. Sci.* **2016**, *9*, 478.
- [6] C. Hu, L. Zhang, Z. J. Zhao, A. Li, X. Chang, J. Gong, *Adv. Mater.* **2018**, *30*, e1705538.
- [7] P. Jiang, Y. Yang, R. Shi, G. Xia, J. Chen, J. Su, Q. Chen, J. Mater. Chem. A **2017**, 5, 5475.
- [8] Y. Lin, L. He, T. Chen, D. Zhou, L. Wu, X. Hou, C. Zheng, *J. Mater. Chem. A* **2018**, *6*, 4088.
- [9] Y. Liu, S. Liu, Y. Wang, Q. Zhang, L. Gu, S. Zhao, D. Xu, Y. Li, J. Bao, Z. Dai, *J. Am. Chem. Soc.* **2018**, *140*, 2731.
- [10] Y. Pan, K. Sun, S. Liu, X. Cao, K. Wu, W. C. Cheong, Z. Chen, Y. Wang, Y. Li, Y. Liu, D. Wang, Q. Peng, C. Chen, Y. Li, *J. Am. Chem. Soc.* **2018**, *140*, 2610.
- [11] Z. Pu, I. S. Amiinu, Z. Kou, W. Li, S. Mu, Angew. Chem. Int. Ed. 2017, 56, 11559.
- [12] L. Shao, H. Sun, L. Miao, X. Chen, M. Han, J. Sun, S. Liu, L. Li, F. Cheng, J. Chen, *J. Mater. Chem. A* **2018**, *6*, 2494.
- [13] Y. Shen, Y. Zhou, D. Wang, X. Wu, J. Li, J. Xi, Adv. Energy Mater. 2018, 8, 1701759.
- [14] M. Q. Wang, C. Ye, H. Liu, M. Xu, S. J. Bao, *Angew. Chem. Int. Ed.* **2018**, *57*, 1963.
- [15] Z. Xiao, Y. Wang, Y.-C. Huang, Z. Wei, C.-L. Dong, J. Ma, S. Shen, Y. Li, S. Wang, *Energ. Environ. Sci.* **2017**, *10*, 2563.
- [16] H. Yan, Y. Xie, Y. Jiao, A. Wu, C. Tian, X. Zhang, L. Wang, H. Fu, *Adv. Mater.* **2018**, *30*, 1704156.
- [17] L. Yu, H. Zhou, J. Sun, F. Qin, F. Yu, J. Bao, Y. Yu, S. Chen, Z. Ren, *Energ. Environ. Sci.* **2017**, *10*, 1820.
- [18] C. Zhu, A. L. Wang, W. Xiao, D. Chao, X. Zhang, N. H. Tiep, S. Chen, J. Kang, X. Wang, J. Ding, J. Wang, H. Zhang, H. J. Fan, *Adv. Mater.* **2018**, *30*, e1705516.
- [19] Z. Zhuang, Y. Li, Z. Li, F. Lv, Z. Lang, K. Zhao, L. Zhou, L. Moskaleva, S. Guo, L. Mai, *Angew. Chem. Int. Ed.* **2018**, *57*, 496.
- [20] L. Zhang, Y. Jia, H. Liu, L. Zhuang, X. Yan, C. Lang, X. Wang, D. Yang, K. Huang, S. Feng, X. Yao, *Angew. Chem. Int. Ed.* **2019**, *58*, 9404.
- [21] K. Sun, L. Zeng, S. Liu, L. Zhao, H. Zhu, J. Zhao, Z. Liu, D. Cao, Y. Hou, Y. Liu, Y. Pan, C. Liu, *Nano Energy* **2019**, *58*, 862.
- [22] T. Ouyang, Y. Q. Ye, C. Y. Wu, K. Xiao, Z. Q. Liu, *Angew. Chem. Int. Ed.* **2019**, *58*, 4923.
- [23] R. Ye, Y. Liu, Z. Peng, T. Wang, A. S. Jalilov, B. I. Yakobson, S. H. Wei, J. M. Tour, *ACS Appl. Mater. Inter.* **2017**, *9*, 3785.

- [24] J. Mahmood, F. Li, S. M. Jung, M. S. Okyay, I. Ahmad, S. J. Kim, N. Park, H. Y. Jeong, J. B. Baek, *Nat. Nanotechnol.* **2017**, *12*, 441.
- [25] J. Xu, T. Liu, J. Li, B. Li, Y. Liu, B. Zhang, D. Xiong, I. Amorim, W. Li, L. Liu, *Energ. Environ. Sci.* **2018**, *11*, 1819.
- [26] J. Mao, C. T. He, J. Pei, W. Chen, D. He, Y. He, Z. Zhuang, C. Chen, Q. Peng, D. Wang, Y. Li, *Nat. Commun.* **2018**, *9*, 4958.
- [27] J. N. Tiwari, A. M. Harzandi, M. Ha, S. Sultan, C. W. Myung, H. J. Park, D. Y. Kim, P. Thangavel, A. N. Singh, P. Sharma, S. S. Chandrasekaran, F. Salehnia, J. W. Jang, H. S. Shin, Z. Lee, K. S. Kim, *Adv. Energy Mater.* **2019**, *9*, 1900931
- [28] B. Lu, L. Guo, F. Wu, Y. Peng, J. E. Lu, T. J. Smart, N. Wang, Y. Z. Finfrock, D. Morris, P. Zhang, N. Li, P. Gao, Y. Ping, S. Chen, *Nat. Commun.* **2019**, *10*, 631.
- [29] W. Li, Y. Liu, M. Wu, X. Feng, S. A. T. Redfern, Y. Shang, X. Yong, T. Feng, K. Wu, Z. Liu, B. Li, Z. Chen, J. S. Tse, S. Lu, B. Yang, *Adv. Mater.* **2018**, *30*, e1800676.
- [30] J. Su, Y. Yang, G. Xia, J. Chen, P. Jiang, Q. Chen, Nat. Commun. 2017, 8, 14969.
- [31] J. Wang, Z. Wei, S. Mao, H. Li, Y. Wang, Energ. Environ. Sci. 2018, 11, 800.
- [32] J. N. Tiwari, N. K. Dang, S. Sultan, P. Thangavel, H. Y. Jeong, K. S. Kim, Nat. Sustain. 2020, 3, 556.
- [33] A. M. Harzandi, S. Shadman, M. Ha, C. W. Myung, D. Y. Kim, H. J. Park, S. Sultan, W.-S. Noh, W. Lee, P. Thangavel, W. J. Byun, S.-h. Lee, J. N. Tiwari, T. J.
- Shin, J.-H. Park, Z. Lee, J. S. Lee, K. S. Kim, Appl. Catal. B 2020, 270, 118896.
- [34] Y. Liu, X. Li, Q. Zhang, W. Li, Y. Xie, H. Liu, L. Shang, Z. Liu, Z. Chen, L. Gu, Z. Tang, T. Zhang, S. Lu, Angew. Chem. Int. Ed. 2020, 59, 1718.
- [35] X. Wang, L. Bai, J. Lu, X. Zhang, D. Liu, H. Yang, J. Wang, P. K. Chu, S. Ramakrishna, X. F. Yu, Angew. Chem. Int. Ed. 2019, 58, 19060.
- [36] Y. Liu, Y. Yang, Z. Peng, Z. Liu, Z. Chen, L. Shang, S. Lu, T. Zhang, Nano Energy 2019, 65, 104023.
- [37] J. Zhang, P. Liu, G. Wang, P. P. Zhang, X. D. Zhuang, M. W. Chen, I. M. Weidinger, X. L. Feng, *J. Mater. Chem. A* **2017**, *5*, 25314.